

Gradient Technique Theory: Tracing magnetic field and obtaining magnetic field strength

ALEX LAZARIAN,^{1,2} KA HO YUEN,³ AND DMITRI POGOSYAN^{4,5}

¹*Department of Astronomy, University of Wisconsin-Madison, USA*

²*Centro de Investigación en Astronomía, Universidad Bernardo O'Higgins, Santiago, General Gana 1760, 8370993, Chile*

³*Theoretical Division, Los Alamos National Laboratory, Los Alamos, NM 87545, USA*

⁴*Department of Physics, University of Alberta, Edmonton, Canada*

⁵*Korea Institute for Advanced Studies, Seoul, Republic of Korea*

(Received June 4, 2024)

Submitted to ApJ

ABSTRACT

The gradient technique is a promising tool with theoretical foundations based on the fundamental properties of MHD turbulence and turbulent reconnection. Its various incarnations use spectroscopic, synchrotron, and intensity data to trace the magnetic field and measure the media magnetization in terms of Alfvén Mach number. We provide an analytical theory of gradient measurements and quantify the effects of averaging gradients along the line of sight and over the plane of the sky. We derive analytical expressions that relate the properties of gradient distribution with the Alfvén Mach number M_A . We show that these measurements can be combined with measures of sonic Mach number or line broadening to obtain the magnetic field strength. The corresponding technique has advantages to Davis-Chandrasekhar-Fermi way of obtaining the magnetic field strength.

Keywords: Interstellar magnetic fields (845); Interstellar medium (847); Interstellar dynamics (839);

1. INTRODUCTION

The magnetic field is an important player in most astrophysical processes (e.g., Mestel & Spitzer 1956; Galli et al. 2006; Mouschovias et al. 2006; Johns-Krull 2007) and therefore it is really important to have ways of studying magnetic fields from observations. In terms of magnetic field tracing, the polarization arising from aligned dust (see Andersson et al. 2015a) as well as synchrotron polarization (see e.g. Lazarian & Yuen 2018a) provide the main avenues of research (see Chepurnov & Lazarian 2010). The development of new ways of studying magnetic fields is essential for understanding the complex dynamics of multiphase interstellar media with ubiquitous magnetic fields. Therefore, several techniques, e.g. Goldreich & Kylafis effect (1981), that uses polarization from molecular lines and the one employing ground state alignment (GSA, Yan & Lazarian 2006, 2007, 2008) have been put forward.

In view of astrophysical flows with large Reynolds numbers, the magnetic fields are turbulent (see Elmegreen & Scalo 2004; McKee & Ostriker 2007; Yuen et al. 2022). The evidence of turbulent magnetic field is coming from observations of density structure of the interstellar medium (e.g. Armstrong et al. 1995; Chepurnov & Lazarian 2009; Ho et al. 2023; Habegger et al. 2024, see review from Yuen et al. (2024)) and velocity fluctuation studies (Larson 1981; Heyer & Brunt 2004; Chepurnov & Lazarian 2010; Chepurnov et al. 2015), synchrotron polarization studies (Zhang et al. 2020a; Pavaskar et al. 2024). The magnetic field makes the turbulence anisotropic, and this was proposed as a way to study the magnetic field Lazarian et al. (2002); Esquivel & Lazarian (2005); Heyer et al. (2008); Lazarian & Pogossyan (2012).

Recently, based on the theory of MHD turbulence and turbulent reconnection (Goldreich & Sridhar 1995, henceforth GS95, Lazarian & Vishniac 1999, henceforth LV99, see also a monograph by Beresnyak & Lazarian 2019) a Gradient Technique of magnetic field tracing was introduced. This technique employs the fact that in MHD turbulence, the gradients of the velocity and magnetic field amplitudes are directed perpendicular to the local direction of the magnetic field. The technique was developed to study velocity gradients (González-Casanova & Lazarian 2017; Yuen & Lazarian 2017a,b; Lazarian & Yuen 2018b,a) but later ex-

alazarian@facstaff.wisc.edu

kyuen@lanl.gov

pogosyan@ualberta.ca

panded to studies of gradients of different nature, most notable branches being Synchrotron Intensity Gradients (SIGs, Lazarian et al. 2017), Synchrotron Polarization Gradients (SPGs, Lazarian & Yuen 2018a) as well as Intensity Gradients (IGs, Yuen & Lazarian 2017b; Hu et al. 2019a; Ho & Lazarian 2023). In addition, Faraday Rotation Gradients (FRGs) and Dust Polarization Gradients (DPGs) were also discussed in Lazarian & Yuen (2018a). In this paper, we provide a formal mathematical theory of these gradients and compare the properties of gradient tracing with that of polarisation measurements. In addition, in Lazarian et al. (2018); Yuen & Lazarian (2020a,b), it was demonstrated that the properties of the gradient distribution can be successfully employed to measure the sonic and Alfvén Mach number, key input parameters that determine the properties of magnetized turbulence.

The subsequent papers successfully applied the gradient technique to studies of magnetic fields both in diffuse media and molecular clouds (see Hu et al. 2021; Hu & Lazarian 2023a). The velocity gradients have also demonstrated their power in predicting the foreground polarization from galactic dust (Hu et al. 2020b; Lu et al. 2020). However, progress was primarily achieved through empirical studies of gradients, which always have disadvantages. This motivates our present formal mathematical study of the properties of gradients in this paper. In particular, it is important to quantify how the ability of gradients to trace magnetic fields and measure magnetization changes with the averaging along the line of sight procedure and the change of the sub-block size. The corresponding theoretical advances can help to develop reliable magnetic field study procedures. However, the major focus for the practical applications of the theory in this paper is using gradients to obtain the strength of the magnetic field from the properties of the gradient distribution in the sub-blocks. In other words, while the study in Lazarian et al. (2018) provides an empirical way to obtain M_A , which is of the order of the ratio of the magnetic field fluctuation to its mean value, the theory can provide analytical predictions for this dependence. When combined with line width broadening or other ways of evaluating the sonic Mach number of the turbulence, one gets a new way of obtaining magnetic field strength.

Traditionally, by the magnetic field is measured by combining the polarization and spectral linewidth. The corresponding technique proposed in Davis (1951) and Chandrasekhar & Fermi (1953) is termed Davis-Chandrasekhar-Fermi technique (henceforth DCF technique). It uses dust polarization to trace the direction of the magnetic field and spectral linewidth to measure the velocity dispersion corresponding to the dispersion in magnetic field directions. The DCF technique was later studied numerically and improved in several of subsequent publications (e.g. Heitsch et al. 2001; Crutcher 2004; Houde 2004; Girart et al. 2006; Falceta-Gonçalves et al. 2008, Cho & Yoo (2016)). These improvements did not change the essence of the technique. Based on the measurements of dispersions of both magnetic field and velocities, the DCF technique is affected by large-

scale shear velocities and the variations of magnetic field directions not directly related to the Alfvénic motions.

An attempt to use the local measures of magnetic field and velocities to obtain the detailed distribution of magnetic field strength and remove the irrelevant large-scale contribution is made in Lazarian et al. (2022, **Paper I**). The approach, named the Differential Measure Analysis (DMA), employs the theory of MHD turbulence to obtain the magnetic field strength by combining the polarization data with spectroscopic data.

This paper explores the possibility of obtaining the magnetic field strength without using polarization data while using gradients instead. This study capitalizes on our earlier studies of media magnetization using gradients. For instance, Velocity Channel Maps provide a way of obtaining both the maps of magnetic field directions using a new Velocity Channel Gradient (VChG) technique (Lazarian & Yuen 2018b) and the Alfvén Mach number (Lazarian et al. 2018). The latter can be obtained on the scale of the data sub-block employed for calculating a single gradient vector within the gradient technique. Using this magnetization, obtaining the magnetic field strength using the same spectroscopic data is possible. Naturally, this approach is synergistic with the DCF and the DMA and has several advantages, which are discussed in this paper.

The magnetization can be successfully obtained with velocity gradients and other types of gradients (Carmo et al. 2020). This opens a way to obtain magnetic field strength with the different data sets that have never been employed for such purposes follows, §2 discusses the essence of the gradient technique. We discuss our numerical setup in §3. In §4, we review the different observables used in the gradient technique. In §5 we formulate the analytical theory gradient statistics dispersions, and introduce a quantity J_2 mimicking circular dispersion in polarization statistics that is shown to be connected to the underlying turbulence structures. In §6, we employ the actual MHD turbulence model to give an estimate of J_2 as functions of Alfvénic Mach number. In §7 we discuss the measures that can be obtained from observations, and the corresponding statistical error estimates. In §8 we present the numerical results verifying the analytical relations predicted in §7. In §9, we discuss the new opportunities based on the development of the analytical theory of gradients. In §10 we discuss the implication of our results, and in §11 we conclude our paper.

2. ALFVÉNIC COMPONENT OF MHD TURBULENCE AND GRADIENT TECHNIQUE

MHD turbulence in sub-Alfvénic and trans-Alfvénic regimes can be presented as a superposition of cascading Alfvén, slow and fast modes (Goldreich & Sridhar 1995; Lithwick & Goldreich 2001; Cho & Lazarian 2002, 2003; Makwana & Yan 2020; Ho & Lazarian 2021; Zhao et al. 2024b,a; Pavaskar et al. 2024). The small-scale Alfvénic fluctuations are marginally affected by their interaction with fast and slow modes (Cho & Lazarian 2002). The Alfvénic

motions are most important for the Gradient Technique and, in what follows, we focus on the Alfvénic turbulence.

2.1. Scaling of eddies in local system of reference

The Gradient Technique (GT) is a technique that employs the properties of MHD turbulence to study magnetic field from observational data. These properties include the anisotropy of velocity and magnetic field fluctuations in the MHD cascade as well as the alignment of these fluctuations with the *local* direction of magnetic field. The latter property is absolutely crucial for the ability of the GT to trace dynamically important magnetic field.¹

The well-accepted hydrodynamic Kolmogorov turbulence (Kolmogorov 1941) can be understood using a mental picture of an eddy cascade. Traditionally, MHD turbulence was considered a wave-type phenomenon, similar to acoustic turbulence (Iroshnikov 1963; Kraichnan 1965) with Alfvénic waves having isotropic distribution. This was shown to be an incorrect picture (Montgomery & Turner 1981, GS95). Note that further, we focus on the Alfvénic turbulence cascade only, as this cascade determines the properties of gradients we deal with. The separation of this cascade from the other two MHD motions is possible because the back-reaction of slow and fast modes of the Alfvénic cascade is marginal in the strong Alfvénic turbulence regime (GS95, Cho et al. 2002, Yuen et al. (2023), see also appendix of Pavaskar et al. (2024)). Thus, the scaling properties of Alfvénic cascade stay unaltered in the compressible media in good agreement with numerical calculations (Cho & Lazarian 2003).

The anisotropic distribution in GS95 picture corresponds to Alfvénic wave vectors getting perpendicular to magnetic field. The corresponding motions are equivalent to eddies according to LV99. The eddy motions were considered impossible in the presence of dynamically important magnetic field. However, the theory of turbulent reconnection (LV99, see Lazarian et al. 2020 for a review) predicts that the magnetic field reconnection happens within one eddy turnover time. This enables unconstrained eddy motions in the direction perpendicular to the magnetic field. As a result, the Kolmogorov picture of turbulence is revived, but with the restriction that the eddy cascade is expected to involve only in the eddies with rotation axes aligned with the direction of magnetic field that surrounds the eddies.

Naturally, the magnetic field in question is those involved in the Alfvénic motion, i.e. the field that percolates the eddies. This is the *local* direction of magnetic field, which is an important advance in understanding Alfvénic cascade. In other words, due to turbulent reconnection, the turbulent motions perpendicular to the magnetic field are not constrained by the back-reaction of magnetic field. This presents the favorable way of turbulent cascading with most energy concen-

trated in eddies rotating perpendicular to the *local* direction of the magnetic field.² Dealing exclusively with Alfvénic turbulence simplifies our further treatment as velocities and magnetic field are related through the Alfvénic relations. Further, in particular in §9 we discuss complicated situations involving non-Alfvénic turbulence.

Accepting the natural constraint that eddies perform the motions that minimize the magnetic field bending, i.e. that due to fast reconnection they easily mix up magnetic field around them in the perpendicular direction, one can get the Kolmogorov-type condition for such perpendicular Alfvénic motions

$$v_l^2/t_{cas,l} = const, \quad (1)$$

where v_l is the velocity of perpendicular to magnetic field eddies and the scale l_\perp and $t_{cas,l}$ is the energy cascading time, i.e. time of the energy transfer from a scale l_\perp scales to a smaller eddy. We use the symbol \perp to explicitly reflect the fact that the cascade involves "perpendicular" eddies. For unconstrained energy transfer from scale to scale, the cascading time is similar to the Kolmogorov turbulence

$$t_{cas,l} \approx \frac{l_\perp}{v_l} \quad (2)$$

The eddies, however, can change their parallel scale l_\parallel . Indeed, the magnetic field mixing with the period l_\perp/V_i induces a wave with a period l_\parallel/V_A , where V_A is the Alfvén velocity. The latter condition, i.e.

$$l_\perp/V_i \approx l_\parallel/V_A, \quad (3)$$

was termed *critical balance* in the GS95 theory of MHD turbulence.³ However, in the latter study the critical balance was derived for the corresponding parallel and perpendicular scales obtain in relation to the *mean* magnetic field rather than to the *local* magnetic field. The subsequent studies (Cho & Vishniac 2000; Maron & Goldreich 2001; Cho & Lazarian 2002) testified that the critical balance and the relations between the l_\perp and l_\parallel that follow from combining Eqs. (1,2) and (3), i.e.

$$l_\parallel \sim l_\perp^{2/3}, \quad (4)$$

are valid only if \parallel and \perp scales are calculated in terms of the *local direction of magnetic field*. It follows naturally from our presentation of Alfvénic cascade that the scaling of eddy

¹ If magnetic field is not dynamically important, it can be advected by velocity motions and passively reflect the statistics of velocity fluctuations. Thus the velocity gradients can trace the magnetic field even in this case. However, we do not consider this situation in the present paper.

² A common misconception about the MHD theory is related to the fact that the concept of the local direction of the magnetic field is not a part of the original GS95 idea. This concept of local magnetic field direction was introduced and proven numerically in Cho & Vishniac (2000) and subsequent studies, e.g., (Maron & Goldreich 2001; Cho & Lazarian 2002).

³ The critical balance assumes that in Eq. (3) it is l_\parallel rather than the injection scale L_{inj} . If this is not true, the cascade is modified. The eddies cannot freely mix and the turbulence in the *weak MHD turbulence* regime with $l_\parallel = L_{inj}$ and perpendicular to magnetic field motions scaling $v_l \sim l^{1/2}$ (GS95, Galtier et al. 2000. See also Mallet et al. 2015; Meyrand et al. 2018 for proofs of critical balance.). This does not change the picture for the gradient studies as the motions are still perpendicular to magnetic field.

velocities is Kolmogorov-type (see Eq. (1), i.e.

$$v_l \sim l^{1/3} \text{ and } b_l \sim l^{1/3} \quad (5)$$

where b_l is the fluctuation of magnetic field.

Apart from Alfvénic motions, slow and fast modes are present in MHD turbulence. The slow modes are present even in the limit of incompressible turbulence and they follow the scaling of Alfvén modes (GS95, Cho & Lazarian 2002, 2003; Lithwick & Goldreich 2001). The fast modes are present in compressible MHD turbulence and it was demonstrated in Cho & Lazarian (2002, 2003) that that provide an isotropic cascade similar to the acoustic turbulence. For magnetic field tracing with the GT, the properties of Alfvén and slow modes are employed. The energy of those usually dominates the energy in the fast modes (see Cho & Lazarian 2002). For subsonic turbulence slow modes dominate the formation of density fluctuations and therefore $\rho_l \sim l_\perp^{1/3}$ and are elongated with the axis ratio scaling given by Eq. (4). The situation is more complicated, however, for supersonic turbulence where the shocks distort significantly the density structure within MHD turbulence (see Beresnyak et al. 2005; Kowal et al. 2007).

2.2. Dependence on magnetization

All the considerations above apply to sub-Alfvénic, i.e., the magnetic field fluctuations δB that are less than the underlying regular magnetic field B_0 . For Alfvénic motions, one can define the Mach number

$$M_A \equiv \frac{\delta B}{B_0} \approx \frac{V_{inj}}{V_A}, \quad (6)$$

where V_{inj} is the injection velocity of the Alfvénic cascade. One identifies $M_A < 1$ with sub-Alfvénic turbulence and $M_A = 1$ with the trans-Alfvénic turbulence. If turbulence is super-Alfvénic, i.e. $M_A > 1$, at the injection scale L_{inj} the motions are hydrodynamic-like down to the scale

$$l_A = L_{inj} M_A^{-3}, \quad (7)$$

where the turbulence transfers to the magnetic field-dominated regime. All our arguments about trans-Alfvénic turbulence are applicable provided that use l_A as the effective injection scale of turbulence.

For scales larger than l_A , the magnetic fields are moved by hydrodynamic flows and the gradients of velocities perpendicular to magnetic fields (see Lazarian et al. 2017, Hu et al. 2024). For scales less than l_A , the velocity gradients are similar to the case of trans-Alfvénic turbulence. For this type of turbulence and $M_A < 1$ turbulence, the gradients are also perpendicular to magnetic field (see Lazarian et al. 2018). In the latter case, this is the consequence of the Alfvénic turbulence anisotropy (GS95; Kandel et al. 2016; 2017a, henceforth KLP16, KLP17).

The properties of MHD turbulence depend on magnetization that is measured using the Alfvén Mach number M_A which is the ratio of the turbulent injection velocity V_{inj}

to the Alfvén velocity V_A , i.e. $M_A = V_{inj}/V_A$. For sub-Alfvénic turbulence (i.e. $M_A < 1$) at scales smaller than

$$l_{tr} = L_{inj} M_A^2 \quad (8)$$

the velocity scaling is given by LV99:

$$v_l \approx V_{inj} \left(\frac{l_\perp}{L_{inj}} \right)^{1/3} M_A^{1/3}, \quad (9)$$

where l_\perp is measured in the local system of reference. ⁴ For this case the eddies get more elongated as it is obvious from the exact expression for $M_A < 1$ turbulence scaling at small separations (LV99):

$$l_\parallel \sim L_{inj} \left(\frac{l_\perp}{L_{inj}} \right)^{2/3} M_A^{-4/3}, \quad (10)$$

For larger magnetization, M_A gets smaller and the eddies get more and more elongated. The distribution of the direction of eddies also changes and the corresponding changes can be traced by studying the distribution of the gradient directions. For instance, the empirical study of gradients distribution in Lazarian et al. (2018) revealed that the dispersion of velocity gradients measured within the sub-block employed for averaging changes as a power law of M_A . In this paper we relate this and other measures of velocity and magnetic field gradients with the analytical expectations.

2.3. Properties of gradients and media magnetization

Later in the paper we derive rigorously the properties of gradients according to the statistical theory of MHD turbulence. For readers' reference, it is advantageous to discuss the gradient properties that directly follow from the MHD turbulence scaling.

For Alfvénic motions of the magnetic and velocity fluctuations are symmetric. The corresponding eddies in magnetized turbulence, as we discussed above, are elongated along the local direction of magnetic field and rotate about this direction. The fact that both velocity and magnetic fluctuations exhibit Kolmogorov-type scaling given by Eq. (5) ensures that the gradients of the amplitudes of fluctuations are largest at the smallest scales resolved. For instance, for velocities $\nabla|v_l| \sim v_l/l_\perp \sim l_\perp^{-2/3}$. The fact that both velocity and magnetic field fluctuations take place and are elongated in respect to the *local* direction of magnetic field means that gradients of individual eddies reflect the direction of the magnetic field at the eddy location. Taken together this means that the Alfvénic gradients are tracing magnetic fields similar to the way that aligned grains trace interstellar magnetic fields.

⁴ At separations larger than $L_{inj} M_A^2$ as we mentioned earlier, the turbulence scaling follows the so-called weak cascade (See Santos-Lima et al. 2021), $v_l \approx V_{inj} (l_\perp/L_{inj})^{1/2}$. The gradient studies, however, usually employ small scales as weak turbulence often occupies only a small portion in MHD simulations.

If one measures gradients within a single magnetized eddy, a distribution of gradient directions is obtained. The maximal amplitude of gradients is in the direction perpendicular to the local magnetic field, while the minimal value corresponding to the direction parallel to the magnetic field. The width of the gradient distribution depends on the media magnetization. Indeed, the eddy elongation increases with the media magnetization, i.e. with the decrease of the Alfvén Mach number M_A (see Eq. 10). As a result, the distribution of the gradients measured for an eddy is getting narrower as M_A decreases. In addition, the ratio of the maximal to minimal values of the measured gradients increases with M_A decrease.

The properties of gradients arising from Alfvénic turbulence play the major role in the Gradient Technique (GT). Through sub-block averaging in Yuen & Lazarian (2017a) one identifies the direction of the maximal gradient amplitude, which is perpendicular to the magnetic field. Measuring the properties of the distribution of the gradients within the sub-block, e.g. the width of the distribution, provides a way to obtain M_A (Lazarian et al. 2018).

As Alfvén modes impose their scaling on the slow modes, the properties of gradients that correspond to slow modes are similar to those of Alfvénic eddies. On the contrary, the fast modes have different type of scaling and the anisotropy that arises from those modes was shown in Lazarian et al. (2018) to be orthogonal to that of Alfvén and slow modes. In most cases, the fast mode contribution to gradients is subdominant (Lazarian & Yuen (2018b,a) and therefore we focus in this paper on exploring of the gradients arising from Alfvén and slow modes.

The properties of density gradients vary with the sonic Mach number of the media M_s . At low M_s the density can be passively moved by Alfvén velocity fluctuations and therefore the gradients of density will be similar to the velocity gradients. At the same time, at higher M_s shocks are being produced. Compressions arising from shocks tend to change the directions of gradients and complicate the interpretation of the density gradients in terms of underlying magnetic field⁵

The analytical study of the relation between the underlying properties of turbulence and the observables was started with the statistics of velocity available via channel maps (Lazarian & Pogosyan 2000, henceforth LP00). The analytical description of the relation of M_A and the anisotropy of the observable statistics was obtained in Lazarian & Pogosyan (2012, henceforth LP12) for the case of synchrotron emission fluctuations. Later studies in KLP16 and KLP17 provided the relation of the anisotropies in spectroscopic channel maps and velocity centroids with M_A . These theoretical studies provide the foundations for obtaining the analytical expressions relating M_A with the statistics of the gradients of the observable fluctuations. Importantly, they relate both

the isotropy degree and quadrupole-to-monopole ratio to the Alfvénic Mach number based on the analytical calculations of LP00, suggesting that the Alfvénic Mach number can be obtained from observations by studying the statistics of velocity observables.

3. NUMERICAL SIMULATIONS

The numerical simulations are originated from three numerical codes: ZEUS-MP/3D (Hayes et al. 2006; Clarke 2010), Athena++ (Stone et al. 2020), and an incompressible MHD spectral code "MHDFlows" (Ho 2022). ZEUS-MP/3D approach uses the 2nd order staggered-grid discretization while Athena++ has multiple options, which we are using 3rd order PPM in space and VL2 in time. The difference of discretization method decides how the numerical viscosity scales as a function of grid size Δx . We summarize the simulations in Table 1 in Appendix C. There, incompressible run was done with MHDFlows, models labeled $M_s??M_A??$ use Athena++, and the rest, which are the majority of our simulations, is based on ZEUS-3D.

Our data cubes are three-dimensional, triply periodic, isothermal MHD simulations with periodic force driving via *direct spectral injection* unless specified. Simulations have the injection scale which is one-half of the size of the cube, so that we only have injected eddies at scales $L_{inj}/L_{box} = 1/2$. The driving force is taken to be solenoidal, giving incompressible driving.

The parameters that are employed are V_{inj} is the injection velocity, V_A and V_s that are the Alfvén and sonic velocities respectively. The parameters give two dimensionless combinations, namely, the Alfvén $M_A = V_{inj}/V_A$ and sonic $M_s = V_{inj}/V_s$ Mach numbers. The results of isothermal MHD simulations can be easily transformed to arbitrary units keeping dimensionless parameters M_A, M_s fixed. The chosen M_A and M_s are listed in Table 1. For the case of $M_A < M_s$, the simulations correspond to thermal pressure smaller than the magnetic pressure, i.e. plasma with $\beta/2 = V_s^2/V_A^2 < 1$. Similarly, the case $M_A > M_s$ corresponds to plasma where the thermal pressure dominates, i.e. $\beta/2 > 1$. The simulations are referred in Table 1 by their model name. The ranges of M_s, M_A, β encompass possible scenarios of astrophysical turbulence.

Simulations exhibit the self-similar turbulent cascade which stops at the dissipation scale that is determined by numerical viscosity and resistivity. The existence of this dissipation scale d_{diss} corresponds to the rapid decrease of turbulent velocities. Our theoretical results should only be referred to turbulence within the inertial range and we will defer our discussion on viscous turbulence in later papers.

4. EXAMPLES OF OBSERVATIONAL DATA TO APPLY GRADIENTS

Spectroscopic data: Velocity Gradients Spectroscopic data of line emission (e.g. 21 cm HI line) in frequency direction reflects, through the Doppler effect, the line-of-sight velocities of the emitters. Speaking about velocity gradients we assume the use of the spectroscopic data. If we

⁵ It was shown in Beresnyak et al. (2005) that even in high M_s media the low contrast density fluctuations follow the Alfvénic GS95 scaling.

denote $\rho(\mathbf{X}, v)$ the density of emitters in Position-Position-Velocity space as a function of Plane-Of-Sky (POS) direction $\mathbf{X} = (x, y)$ and the velocity v , the simplest quantity that can be analyzed is the intensity within the velocity channel centered at v_c :

$$I(\mathbf{X}, v_c) \sim \int_{v_c - \delta v/2}^{v_c + \delta v/2} \rho(\mathbf{X}, v) dv, \quad (11)$$

where δv is the width of the channel. The instrument's spectral resolution determines the narrowest available width, but one can also consider synthesized channels and vary the width above the resolution limit. Thermal broadening effectively adds to the width of a channel, blurring the effect of turbulent velocities (see LP00 for the exact criterion, and Yuen & Lazarian 2020a for the case when the thermal width is larger than turbulent velocity). One should note that it is the thermal velocity $\beta_T^{1/2} \equiv \sqrt{k_B T/m}$, m being the mass of atoms, T being the temperature and k_B being the Boltzmann constant, rather than temperature *per se* that matters. Thus, lines from heavier species exhibit less thermal broadening than the ones from lighter species at the same temperature.

When the effective channel width exceeds the typical turbulent velocities, the channel maps are dominated by column density fluctuations. The effect of velocities is enhanced by using velocity centroids, which can be generalized to *reduced centroids* (Lazarian & Yuen 2018b) defined as

$$C_{red}(\mathbf{X}) \propto \int_{\delta v} dv v \rho(\mathbf{X}, v), \quad (12)$$

where the choice of δv can be arbitrary. Conventional (here, un-normalized, following Lazarian & Esquivel 2003) centroids correspond to δv encompassing the full range of the velocities in the line. In this case centroid correlation statistics are not sensitive to thermal broadening (KLP17) (See Appendix of Yuen et al. (2021) for discussions).

If the spectral resolution of the instrument is higher than the thermal velocity, one can get additional information from *sub-thermal centroids* defined as

$$C_{subT}(\mathbf{X}) \propto \int_{\beta_T^{1/2}} dv v \rho(\mathbf{X}, v). \quad (13)$$

These types of centroids can deliver the information on turbulent velocities at small scales that are hidden by the thermal broadening.

From the spectroscopic data, both channel maps and centroids one can construct the measures that are related to the spacial changes of the velocity value in the neighboring points, i.e. with "velocity gradients". In a series of papers (González-Casanova & Lazarian 2017; Yuen & Lazarian 2017a,b; Lazarian et al. 2017; Lazarian & Yuen 2018b) we introduced velocity gradients as a way of tracing magnetic field and prove them as an efficient tracer.

We stress again that the velocity gradients, as other types of gradients that we consider further trace the "local magnetic field around the eddies". It is also important the gradients

of velocity amplitude scale as $v_l/l_\perp \sim l^{-2/3}$, meaning that the maximal gradients are produced by the smallest resolved eddies. Due to this scaling, regular shearing motions do not affect the velocity gradient measurements.

Velocity gradients present a possibility of 3D studies if different molecular lines are used. Indeed, different molecules are produced and survive at different depth in molecular clouds. This opens a possibility of studying magnetic fields in molecular clouds at different depths (Yuen & Lazarian 2017b; Hu et al. 2019c) In addition, galactic rotation provides a way to probe magnetic field at different distances from the observer (González-Casanova & Lazarian 2019). Note, that due to the galactic rotation, velocity gradients can sample magnetic fields in many more clouds in the galactic disc compared to far infrared polarimetry. For the latter, the confusion of emission from different clouds along the line is sight is detrimental.

As we discussed earlier, the gradients in practice should be calculated over a sub-block as proposed in Yuen & Lazarian (2017a). This provides the necessary averaging that is required to reliably determine the gradient direction. The distribution of gradients over the sub-block was identified in Lazarian et al. (2018) as a source of information about media magnetization.

Gradients of velocity-related quantities (e.g. constant density channels, velocity centroids, velocity channels processed by Yuen et al. (2021)) generally have better tracing power on magnetic field than that of density-related quantities (e.g. column density maps). Therefore, both for the successful magnetic field tracing and studying media magnetization, it is advantageous to separate the PPV fluctuations that arise from velocity caustics, i.e. due to the velocity crowding, from the PPV fluctuations arising from the density fluctuations. This problem can be dealt with using the Velocity Decomposition Algorithm (VDA) introduced in Yuen et al. (2021).

In the presence of gravity, it was reported in Yuen & Lazarian (2017b) that the direction of velocity gradients measured by velocity centroids flips 90 degrees becoming parallel to magnetic field. The same effect was also demonstrated in Lazarian & Yuen (2018b) for velocity channel maps. A procedure to account for this effect and successfully trace magnetic field in the star formation regions was introduced in Hu et al. (2019c). However, the application of the VDA shows that the observed flip of the gradients obtained with centroids and velocity channel maps is related to the density effects. The actual 90 degree flip of the velocity gradients takes place on scales that are smaller than those resolved in observations. All in all, even in the presence of gravity, the velocity gradients can be successfully used to trace magnetic field.

Synchrotron Intensities. Similar to the gradients of velocities, the gradients of magnetic field can trace the magnetic field direction. The gradients of synchrotron intensities and synchrotron polarization boil down to magnetic field gradients.

The synchrotron emission depends both on the distribution of relativistic electrons

$$N_e(\mathcal{E})d\mathcal{E} \sim \mathcal{E}^\alpha d\mathcal{E}, \quad (14)$$

with intensity of the synchrotron emission given by the line-of-sight integral

$$I_{\text{sync}}(\mathbf{X}) \propto \int dz B_\perp^\gamma(\mathbf{X}, z) \quad (15)$$

where $B_\perp = \sqrt{B_x^2 + B_y^2}$ is the magnitude of the magnetic field component perpendicular to the LOS z . In general, $\gamma = 0.5(\alpha + 1)$ is a fractional power, a problem successfully addressed in LP12.

Other types of gradients include gradients of Zeeman measure and Faraday rotation gradients Lazarian et al. (2018). The synergy of different types of gradients opens new avenues for studying magnetic fields in multi-phase ISM. For instance, Faraday rotation gradients map the magnetic fields in dense ionized gas, while Synchrotron Intensity gradients have more tenuous halo media along the same lines of sight. The statistics of the aforementioned types of gradients are similar. Thus, we will discuss only gradients of centroids and gradients of synchrotron intensities.

5. GRADIENT THEORY: PLANE OF SKY OBSERVABLES

In this section we develop a theoretical description of the simplest statistics of 2D gradients of projected observables on the sky, namely, the covariance tensor of gradient components σ_{ij} , in relation to the properties of 3D turbulent volume from which the observed signal originates. In particular, we'll show that eigendirections of σ_{ij} matrix give a localized direction of the projected magnetic field, while the level of anisotropy in σ_{ij} can be used to measure the Alfvénic Mach number M_A .

5.1. Statistics of 2D gradients

Let us discuss the mathematical foundations of the gradient methods in application to study of the direction of the magnetic field. We also refer to Appendix A for details.

Observing emission from the turbulent media, one constructs the sky maps of different observables that describe the emission. First of all, this is the intensity of the emission in PPV space, where the position-position \mathbf{X} POS 2D vector and the velocity v coordinate determine position of individual intensities $\rho(\mathbf{X}, v)$, and the related integrated quantities, such as the total intensity and velocity centroids which for optically thin lines are $I_c(\mathbf{X}) \propto \int dv I(\mathbf{X}, v)$ and $C(\mathbf{X}) \propto \int dv v \rho(\mathbf{X}, v)$ respectively (See §4). The maps represent random fluctuating fields. For general exposition, let us denote this 2D signal map as $\Phi(\mathbf{X})$.

The main local statistical measure of the gradient of a 2D field $\Phi(\mathbf{X})$ is the gradient covariance tensor

$$\sigma_{ij} \equiv \langle \nabla_i \Phi(\mathbf{X}) \nabla_j \Phi(\mathbf{X}) \rangle = \nabla_i \nabla_j D(\mathbf{R})|_{\mathbf{R} \rightarrow 0} \quad (16)$$

where \mathbf{R} is the separation between the point at the POS plane. Notice that σ_{ij} is the zero separation limit of the second derivatives of the field structure function

$$D(\mathbf{R}) \equiv \frac{1}{2} \langle (\Phi(\mathbf{X} + \mathbf{R}) - \Phi(\mathbf{X}))^2 \rangle. \quad (17)$$

For a statistically isotropic field, the covariance of the gradients is isotropic, $\sigma_{\nabla_i \nabla_j} = \frac{1}{2} \delta_{ij} \Delta D(R)|_{R \rightarrow 0}$. In the presence of the magnetic field, $D(\mathbf{R})$ of the signal becomes orientation dependent, depending on the angle between \mathbf{R} and the projected direction of the magnetic field. This anisotropy is retained in the limit $\mathbf{R} \rightarrow 0$ and results in non-vanishing traceless part of the gradient covariance tensor

$$\begin{aligned} \sigma_{ij} - \frac{1}{2} \delta_{ij} \sum_{l=1,2} \sigma_{ll} &= \\ &= \frac{1}{2} \begin{pmatrix} (\nabla_x^2 - \nabla_y^2) D(\mathbf{R}) & 2\nabla_x \nabla_y D(\mathbf{R}) \\ 2\nabla_x \nabla_y D(\mathbf{R}) & -(\nabla_x^2 - \nabla_y^2) D(\mathbf{R}) \end{pmatrix}_{\mathbf{R} \rightarrow 0} \neq 0 \end{aligned} \quad (18)$$

As shown in Lu et al. (2020) and Appendix A.1, the eigendirections of this covariance tensor coincide with the direction of local statistical anisotropy of the motions which in MHD turbulence is expected to be given by the local projected direction θ_H of the magnetic field.

$$(\nabla_x^2 - \nabla_y^2) D(\mathbf{R}) = I_2 \cos 2\theta_H \quad (19)$$

$$2\nabla_x \nabla_y D(\mathbf{R}) = I_2 \sin 2\theta_H \quad (20)$$

where the magnitude of the anisotropic part I_2 in relation to the isotropic trace $I_0 = (\nabla_x^2 + \nabla_y^2) D(\mathbf{R})$ is given by the ratio of the quadrupole to monopole moments of the structure function

$$\frac{I_2}{I_0} = 2 \lim_{R \rightarrow 0} \frac{D_2(R)}{D_0(R)} \quad (21)$$

with $D_m(R) = \frac{1}{2\pi} \int d\phi D(R, \phi) e^{-im\phi}$. Thus, the information about magnetic field direction can be recovered by measuring the distributions of the gradients over local patches of 2D sky and finding the eigendirections of σ_{ij} in each of them.

The square of I_2/I_0 in Eq. (21) is related to the ratio of the two rotational invariants of the covariance tensor, that we will denote J_2 ,

$$J_2 = \frac{(\sigma_{xx} - \sigma_{yy})^2 + 4\sigma_{xy}^2}{(\sigma_{xx} + \sigma_{yy})^2} = 4 \left(\lim_{R \rightarrow 0} \frac{D_2(R)}{D_0(R)} \right)^2. \quad (22)$$

The parameter J_2 determines the level of dispersion of the directions of the gradients relative to the eigen-directions of σ_{ij} . This is the quantity that carries information about the level of anisotropy of turbulence processes, and, therefore, on the parameters of the turbulence.

A similar to J_2 parameter is the ratio of the quadrupole D_2 to monopole D_0 moments of the structure function

$$F = \frac{D_2(R)}{D_0(R)} \quad (23)$$

This ratio has appeared in LP12 as a convenient measure of turbulence anisotropy. It was analytically examined for Alfvén, slow, fast modes of MHD turbulence as well for some mixtures of MHD modes for both the synchrotron intensity fluctuations and the measures of fluctuations of intensities within spectroscopic data cube statistics (LP00; KLP16; KLP17). These studies demonstrated that both M_A and the composition of turbulent modes can be studied using the ratio F .

The difference with gradients is that the quadrupole to monopole ratio is evaluated at vanishing lag, i.e. $R \rightarrow 0$. We note that for both Alfvén and slow MHD modes $D_2(R)$ and $D_0(R)$ have the same power-law dependence on the separation R (see Eq. (5) and Cho & Lazarian (2003)). Therefore, if these modes dominate, J_2 dependence on R is very weak.⁶ This makes it possible to relate J_2 to factor F at finite lag

$$J_2(\text{Alfven, Slow}) \approx 4F^2 \quad (24)$$

This equation relates earlier approach of LP12 based on the structure function multipole ratio and the new one based on measuring the gradients.

5.2. Spatial localization of the gradient information

Strictly local statistical measures, such as σ_{ij} at a given sky position, are not accessible in observations, since one needs to average over some region of the sky to simulate the ensemble averaging. In case of a statistically homogeneous measure, the ergodicity principle shows that increasing the volume for averaging allows for ever better determination of statistical values. However, in our case the direction of the magnetic field varies on the sky, therefore statistics of the gradients is not homogeneous. In this situation, determining gradient covariance over the finite patch gives the direction of the projected magnetic field locally averaged over the patch. When choosing the patch size, one needs to balance the loss of resolution and information when increasing the patch size versus the increase of errors due to insufficient statistics if the patch is too small. The choice of the optimal patch size becomes an important parameter of the analysis.

The situation can be modelled by a patch-background split, where within a local patch of scale L_p centered at position \mathbf{X}_p , termed **sub-block** in Yuen & Lazarian (2017a), the signal can be decomposed into short-wave Fourier modes with $K > K_p \approx 1/L_p$ that have approximately homogeneous but anisotropic distribution with the power spectrum $P(\mathbf{K}, \hat{\Lambda}(\mathbf{X}_p))$, while the direction of the magnetic field $\hat{\Lambda}(\mathbf{X}_p)$ has long-wave variations between the patches. Within a patch the formalism of the homogeneous axis-symmetric turbulence can be applied (Oughton et al. 1997, LP12) to the gradients, giving the local direction of the magnetic field via the eigen-direction of the gradient covariance tensor $\theta_H(\mathbf{X}_p)$

⁶ The exact scaling of fast modes is still the issue of debates. It is suggestive that it follows the acoustic cascade $E(k) \sim k^{3/2}$ for low M_s while the spectrum gets steeper, i.e. $\sim k^{-2}$ as M_s increases and shocks are formed (Cho & Lazarian 2003; Kowal & Lazarian 2010; Makwana & Yan 2020).

and the now local parameter $\tilde{J}_2(\mathbf{X}_p)$ expressed via the short-wave part of the power spectrum as

$$J_2(\mathbf{X}_p) = \left(\frac{\int_{K_p}^{\infty} K dK K^2 P_2(K, \hat{\Lambda}_{\mathbf{X}_p}) W_b(K/K_b)}{\int_{K_p}^{\infty} K dK K^2 P_0(K, \hat{\Lambda}_{\mathbf{X}_p}) W_b(K/K_b)} \right)^2 \quad (25)$$

where $P_2(K)$ and $P_0(K)$ are the quadrupole and the monopole moments of the power spectrum determined within the patch at position \mathbf{X}_p , and $\hat{\Lambda}_{\mathbf{X}_p}$ is the unit vector in the direction of the mean magnetic field within the sub-block. The range of scales $K_p < K < K_b$ is bounded by the patch size, $K_p \approx 1/L_p$, and by the beam of the telescope or low-pass post-processing window, W_b , that smooths out fluctuations at very short modes $K > K_b$. Importantly, due to extra K^2 weight, the gradient covariance tensor is primarily determined by the shortest wavelengths $\sim 1/K_b$, which justifies the patch-background split.

One should stress that low pass smoothing of the signal by W_b is critical for practical applications of the gradient techniques. It assures that the limit in Eq. (22) is convergent and, correspondingly, that the measurements of the gradients are stable. In addition, the low-pass filtering should be isotropic as not to modify J_2 by introducing artificial anisotropy. Observations inevitably have low-pass filtering due to finite beam which usually does not resolve turbulent motions on scales less than the turbulence dissipation scale. Numerical simulations, on the other hand, also have intrinsic low-pass filtering corresponding to the numerical dissipation scale K_d , where the spectrum $P(\mathbf{K}, \hat{\Lambda}(\mathbf{X}_p))$ is exponentially suppressed for $K > K_d$. Despite that, it is advantageous in the analysis to deconvolve, as much as possible, this “instrumental” effects and smooth the data with a synthetic, preferably well behaved Gaussian low-pass filter, to maintain the maximum control over the scale and isotropy of the filtering procedure.

Due to different averaging along the line of sight in different patches, two dimensional projected spectra and, therefore $J_2(\mathbf{X}_p)$ may vary significantly from patch to patch. We discuss this issue in the next section.

6. RELATING GRADIENT STATISTICS TO AVERAGE TURBULENCE POWER SPECTRUM

6.1. Accumulation of gradients along the line of sight

Projected 2D gradients are results of the line-of-sight (LOS) integration over depth L of 3D signal

$$\nabla_R \Phi(\mathbf{R}) = \nabla_R \int_0^L dz \phi(\mathbf{R}, z) \quad (26)$$

where LOS coordinate is chosen to be z . Analysing a patch we shall consider only modes with 2D wavelengths on the sky shorter than L_p . Correlation and spectral properties of the gradient, nevertheless, include scales extending past L_p along the LOS. To study how signal accumulates when we integrate over LOS distance $L \geq L_p$, we start by considering a cubical volume of magnetized fluid $L_p \times L_p \times L_p$ which

we will term **c-block**. Within c-block we assume that the turbulence is axis-symmetric with the mean direction of the magnetic field given by the vector λ . Therefore, the analytical description in LP12 applies to a c-block magnetic field. Over larger distances $\hat{\lambda}(z)$ may vary according to long-wave behaviour of the magnetic field. Let us see how the statistic of gradients is determined in this picture.

To use the MHD turbulence description in global system of reference (see LP12), one should consider scales that are sufficiently small either in comparison with L_{inj} or l_A . In fact, in most cases we want to get as high resolution as possible and deal with sub-blocks much less than any of the two scales (see Yuen & Lazarian 2017a). As a result, for our theoretical description, we take the patch size L_p to be sufficiently smaller than either L_{inj} for sub-Alfvénic case or l_A for super-Alfvénic one. In a c-block of volume L_p^3 one can approximate 3D turbulent signal ϕ as anisotropic with a fixed 3D anisotropy direction $\hat{\lambda}$ and described by the power spectrum $P_c(k, \hat{\mathbf{k}} \cdot \hat{\lambda})$. Note that P_c is defined locally to a particular c-block, thus label ‘‘c’’.

First, we shall establish how the gradients are correlated along the line of sight. We are interested only in scaling, so we shall neglect the anisotropic nature of the spectrum, taking it in the model form

$$P_c(k) \approx \langle \phi^2 \rangle k^{-3} (k L_{inj})^{-m} \quad (27)$$

(See Lazarian & Pogosyan 2006) where m is the spectral index, e.g., $m = -2/3$ for Kolmogorov scaling. We compute the trace of the correlation for the gradients smoothed with a Gaussian beam at the beam scale L_b in approximation $L_p \gg L_b$:

$$\begin{aligned} \xi_{\nabla\nabla}(z) &= \pi \int_{1/L_p} K^2 d^2 K e^{-K^2 L_b^2} \int dk_z P_c(K, k_z) e^{ik_z z} \\ &\propto \frac{\langle \phi^2 \rangle}{L_b^2} \left(\frac{L_b}{L_{inj}} \right)^m \tilde{\xi}_{\nabla\nabla}(z/L_b) \end{aligned} \quad (28)$$

where the direct integration gives

$$\begin{aligned} \tilde{\xi}_{\nabla\nabla}(y = z/L_b) &\approx \sqrt{\frac{\pi}{2}} \cos\left(\frac{m}{2}\pi\right) \Gamma[-1-m] \times \\ &\times \left(y^{2+m} + 2^m (2m - y^2) e^{\frac{1}{4}y^2} \Gamma\left[1 + \frac{m}{2}, \frac{1}{4}y^2\right] \right). \end{aligned} \quad (29)$$

This shows that the correlation decreases as $(L_b/z)^{-2+m}$ at LOS distances $z > L_b$. Thus, the gradients are added up in uncorrelated fashion during integration over the depth exceeding the smoothing scale L_b .

This is reflected in the variance of the gradients projected over c-block depth L_p

$$\begin{aligned} \sigma_{ij}(L_p) &\equiv \langle \nabla_{R_1} \Phi(\mathbf{R}_1) \cdot \nabla_{R_2} \Phi(\mathbf{R}_2) \rangle_{R_2 \rightarrow R_1} \\ &= -L_p \int_{-L_p}^{L_p} dz \xi_{\nabla\nabla}(z) \\ &\propto \frac{L_p}{L_b} \langle \phi^2 \rangle (L_b/L_{inj})^m \end{aligned}$$

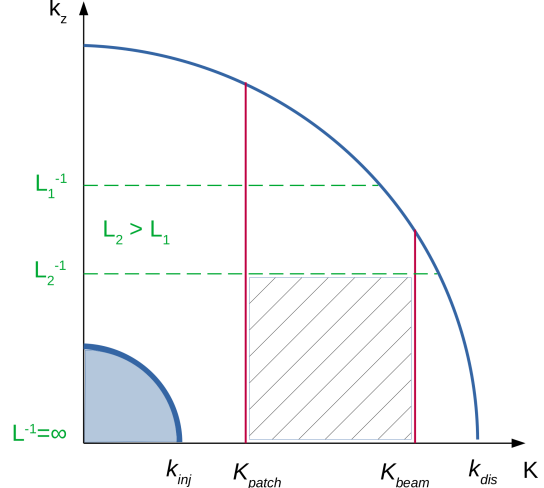


Figure 1. The dashed area is the part of the phase space that contributes to the variance of the gradients, after the line of sight integration is done through the depth $L_2 = L_p$ of the c-block. Here $K_{inj} \sim 1/L_{inj}$, while $K_{patch} \sim 1/L_p$ and $K_{beam} \sim 1/L_b > K_{patch}$. We see that the wavenumber of relevant modes is dominated by sky component $K > k_z$ and modes with wavelengths approaching the injection scale (blue shaded region) have little contribution to the gradient variance. Extending the line-of-sight interaction range shrinks the height of the dashed region, ever improving $k_z = 0$ approximation.

accumulating only linearly with the c-block depth L_p , since $L_p \gg L_b$. Here we point out that L_p appears in the gradient variance only as the depth of a c-block along the LOS. From the point of view of orthogonal scales, gradients have sufficient small scale power to be determined predominantly by the beam scale L_b . Notably, $\langle \phi^2 \rangle (L_b/L_{inj})^m$ can be viewed as a variance of differences of quantity ϕ at separations L_b , i.e. $\langle \Delta\phi(L_b)^2 \rangle$.

Let us now consider anisotropic aspects of the projected gradient variance tensor in a single c-block. This tensor structure in the Fourier space is

$$\begin{aligned} \sigma_{ij}(L_p) &= L_p \int_{-L_p}^{L_p} dz \times \\ &\times \int_{1/L_p}^{\infty} d^2 K K_i K_j e^{-K^2 L_b^2} \int_0^{\infty} dk_z P_c(k, \hat{\mathbf{k}} \cdot \hat{\lambda}) e^{ik_z z} \end{aligned} \quad (30)$$

Line of sight integration through the c-block suppresses all the modes with $k_z > 1/L_p$. Thus, as illustrated in Fig. 1, only $K > 1/L_p$ and $k_z < 1/L_p$ contribute, and one can effectively set k_z to zero in the result

$$\sigma_{ij}(L_p) \approx L_p \int_{1/L_p}^{\infty} d^2 K K_i K_j P_c(K, \hat{\mathbf{k}} \cdot \hat{\lambda}, k_z = 0) \quad (31)$$

(degenerate case when this may not be accurate is when the anisotropy direction is close to the line of sight).

Subsequent c-blocks along z-axis can be considered as having different direction of the magnetic field $\hat{\lambda}(z)$, but uncorrelated gradient signal between the blocks, thus the total variance of projected gradients becoming sum of variances of individual c-blocks, $\sigma_{ij} \approx \sum_c \sigma_{ij}(L_p)$

$$\begin{aligned} \sigma_{ij} &\approx \int d^2 K K_i K_j \left[\sum_c L_p P_c(K, \hat{k} \cdot \hat{\lambda}(z), k_z = 0) \right] \\ &\approx L \int d^2 K K_i K_j \overline{P(\mathbf{K})} \end{aligned} \quad (32)$$

where overline designates averaging over the directions $\hat{\lambda}$ takes over the integration depth L ,

$$\overline{P(\mathbf{K})} = \frac{1}{L} \int_0^L dz P_c(K, \hat{k} \cdot \hat{\lambda}(z), k_z = 0) \quad (33)$$

i.e the effective 2D spectrum of projected gradients is the average of individual c-block spectra over the directions of the local to c-block magnetic field. Note that P_c is defined only within a c-block where we can assume LP12 description. The result in Eqs. (32,33) can be also described using polarization analogy. Covariance σ_{ij} has the same rotational properties as the linear polarization tensor. Introducing the effective Stokes parameters for a c-block as $Q = \sigma_{xx} - \sigma_{yy}$ and $U = 2\sigma_{xy}$, we see that these Q and U are simply additive as we sum c-blocks along the line of sight.

6.2. Averaging of power spectrum along the LOS in strong turbulence regime

For sub-Alfvénic turbulence, the directions of magnetic field in individual c-blocks along the line of sight are correlated over the turbulence injection scale L_{inj} . Within this scale, both the regime of weak at $l > l_{tr} = L_{inj} M_A^2$ and strong at $l < l_{tr}$ sub-Alfvénic turbulence is present. On scales $l \gg L_{inj}$ the magnetic field fluctuations are not correlated and add in a random walk fashion. The rms angular difference of the magnetic field directions between c-blocks separated by more than L_{inj} is of the order of the Alfvén Mach number M_A .

For super-Alfvénic turbulence $M_A > 1$, the correlation length of magnetic field is determined by a smaller scale $l_A = L M_A^{-3}$. The magnetic field on scales larger than l_A is uncorrelated and the variation of the magnetic field direction from one volume $l_A \times l_A \times l_A$ to another similar volume is of the order of unity.

For sub-Alfvénic turbulence in strong regime, the correlated rms deviations of c-block field directions λ over the distance l_{\perp} measured perpendicular to the mean magnetic field is characterized by the angle α :

$$\tan \alpha \approx \frac{l_{\perp}}{l_{\parallel}} \approx \left(\frac{l_{\perp}}{L_{inj}} \right)^{1/3} M_A^{4/3}, \quad (34)$$

which can be seen from Eq. (10). This scaling proceeds up to the transitional scale between the weak and strong cascades $l_{tr} = L_{inj} M_A^2$ (Lazarian 2006).⁷

To estimate the LOS averaging of a c-block spectrum in Eq. (33) one need a specific model for the power distribution P_c in a c-block. Following LV99, in the strong turbulence regime at scales $k L_{inj} > M_A^{-2}$, the peak of power distribution lies at wave angles to the local direction of the magnetic field given by $\cos \theta_k = \hat{k} \cdot \hat{\lambda} \approx v_k / V_A$ where v_k is the rms turbulent velocity at the scale $k = 1/l$ (note that v_k / V_A can be understood as a local Alfvén Mach number). Relating v_k to the velocity v_{inj} at the injection scale $k \approx L_{inj}^{-1}$ using Eq. (9), we have $\cos \theta_k \sim (k L_{inj})^{-1/3} M_A^{4/3}$ where it is taken into account that strong turbulence regime is replaced by weak turbulence at $1 < k L_{inj} < M_A^{-2}$. Thus, the power is strongly peaked for wavevector directions almost perpendicular to the magnetic field, $|\cos \theta_k| < M_A^2$, though strictly perpendicular waves are somewhat disfavoured. The shorter the wavelength, the more concentrated the power is in the perpendicular direction. At the level of individual c-block, the dispersion of directions will be dominated by the longest wavelengths present, i.e., the ones of the scale of the c-block $k \sim L_p^{-1}$. Thus, similar to LP12 we can expect that in the regime of strong turbulence,

$$P_c(\mathbf{k}) \propto k^{-11/3} \exp \left(- \frac{(L_{inj}/L_p)^{1/3} |\hat{\mathbf{k}} \cdot \hat{\lambda}|}{M_A^{4/3}} \right) \quad (36)$$

provides an adequate description for power distribution between differently oriented Alfvén and slow modes. Note, however, that to use this scaling, the size of the c-block should be sufficiently small, $L_p < L_{inj} M_A^2$.

Adding contributions from different c-blocks along the line of sight amounts to convolution of the angular part of the $k_z = 0$ sky projection c-block power $P_c(\mathbf{k})$ with distribution of the 3D direction of the magnetic-field $\hat{\lambda}$ around the global direction of the magnetic field $\hat{\lambda}_0$. We will model the distribution of λ direction by assuming that the perturbations in the magnetic field $\delta \mathbf{b}$ are Gaussian and distributed in 3D isotropically around global λ_0 direction with $\langle \delta b^2 \rangle / B_0^2 = M_A^2$, which gives

$$\mathcal{P}(\theta_{\hat{\lambda}}) = \frac{1}{2\pi} \left(1 + \frac{2 \cos^2 \theta_{\hat{\lambda}}}{M_A^2} \right) \exp \left[- \frac{\sin^2 \theta_{\hat{\lambda}}}{M_A^2} \right] \quad (37)$$

where $\theta_{\hat{\lambda}} \in (0, \pi/2)$ is the angle measuring the deviation of the headless vector $\hat{\lambda}$ from $\hat{\lambda}_0$ axis. Let us note that in the

⁷ At the scale l_{tr} the scaling of turbulent motions changes and, as a result, the change of the angle behaves as

$$\tan \alpha \approx \frac{v_l}{V_A} \approx \left(\frac{l_{\perp}}{L_{inj}} \right)^{1/2} M_A, \quad (35)$$

where we used the scaling of the weak turbulence $v_l \approx M_A V_A (l_{\perp}/L_{inj})^{1/2}$.

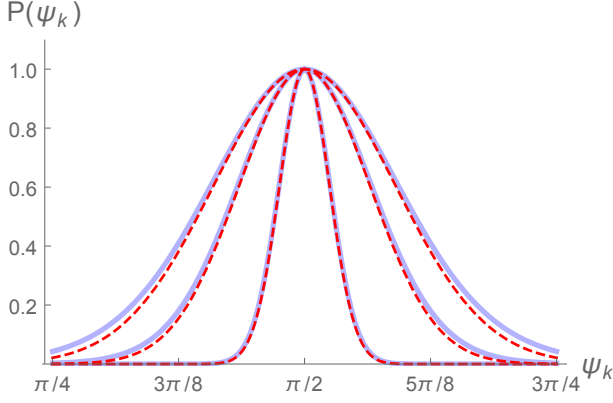


Figure 2. Normalized angular dependence of the 2D spectrum of the gradients as given by Eq. (38) (blue, solid) versus the analytical fit of Eq. (39) (red, dashed). Three sets of curves correspond to $M_A = 0.1, \gamma = \pi/2$ (the most narrow), $M_A = 0.1, \gamma = \pi/8$ and $M_A = 0.4, \gamma = \pi/2$ (the widest, which starts showing some deviations of the fit). $L_p = 0.01 L_{inj}$ for all cases.

isotropic limit $M_A \rightarrow \infty$, $\langle \cos^2 \theta_{\hat{\lambda}} \rangle \rightarrow 1/3$ with respect to an *arbitrary* axis. In the opposite limit, $M_A \rightarrow 0$, $\mathcal{P}(\theta_{\hat{\lambda}}) \rightarrow \delta_D(\theta_{\hat{\lambda}})$ and $\hat{\lambda} \rightarrow \hat{\lambda}_0$ with $\langle \sin^2(\theta_{\hat{\lambda}}) \rangle \sim M_A^2$.

Combining Eq. (36) and Eq. (37) gives the following expression for the angular part of the line-of-sight averaged power spectrum

$$\overline{P(\mathbf{K})} \propto \frac{1}{2\pi} \int d\Omega_{\hat{\lambda}} \exp\left(-\frac{(L_{inj}/L_p)^{1/3}}{M_A^{4/3}} |\hat{\mathbf{K}} \cdot \hat{\lambda}|\right) \times \left(1 + 2\frac{(\hat{\lambda} \cdot \hat{\lambda}_0)^2}{M_A^2}\right) \exp\left(-\frac{1 - (\hat{\lambda} \cdot \hat{\lambda}_0)^2}{M_A^2}\right) \quad (38)$$

For $M_A < 1$ and $L_p/L_{inj} < M_A^2$ the first exponential term is narrower than the second and can be treated as a Dirac δ -function. The resulting distribution of \mathbf{K} directions is then largely determined by the local magnetic field's direction variations $\hat{\lambda}$ itself. To approximate the integral over the directions of $\hat{\lambda}$ we notice that the maximum contribution comes from $\hat{\lambda}$'s that are both perpendicular to $\hat{\mathbf{K}}$ and lie in the plane spanned by $\hat{\mathbf{K}}$ and $\hat{\lambda}_0$ vectors. For such $\hat{\lambda}$'s we have $(\hat{\lambda} \cdot \hat{\lambda}_0)^2 = 1 - \cos^2 \psi_k \sin^2 \gamma$ where ψ_k is the angle between \mathbf{K} and 2D projection of the mean field direction $\hat{\Lambda}_0$, so that $\cos \psi_k = \hat{\mathbf{K}} \cdot \hat{\Lambda}_0$. Substituting this in Eq. (38) gives

$$\overline{P(\mathbf{K})} \approx \exp\left(-\frac{(\psi_k \pm \pi/2)^2}{(M_A/\sin \gamma)^2}\right) \quad (39)$$

in the approximation of small $\cos \psi_k$ that has two solutions $\cos^2 \psi_k \approx (\psi_k \pm \pi/2)^2$. Our numerical integration suggests that Eq. (39) is an excellent approximation for $M_A/\sin \gamma < \pi/8$.

In Fig. 2 we plot the comparison of Eq. (39) with Eq. (38) as a function of $M_A/\sin \gamma$. We see that the approximation of

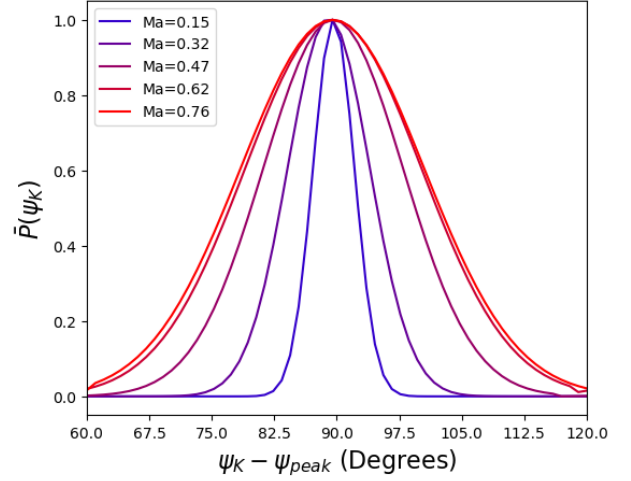


Figure 3. Angular dependence of the 2D power spectrum $P(\psi_K)$ as a function of ψ_K (recentered with respect to ψ_{center}) in the projected maps from five selected simulation data (huge-0 to huge-4) with only Alfvén modes. Due to the noises of the angular spectrum, the presented curves are the Gaussian fits of the angular spectrum instead of the raw data itself.

Eq. (39) has not much visible differences from the exact form in Eq. (38). In Fig. 3 we show normalized angular power distribution obtained from the synthetic observational maps from pure Alfvén modes extracted in numerical simulations “huge-0” to “huge-4” with different M_A . We can see that Fig. 2 and Fig. 3 has very similar trend as M_A grows.

6.3. Theoretical approximation for J_2 parameter

To summarize, we have demonstrated that the covariance matrix of projected gradients in a $L_p \times L_p$ sub-block on a sky is determined by the spectrum that has a concentration of power at wavemodes orthogonal to the mean projected direction $\hat{\Lambda}_0$ of the magnetic field within the line-of-sight cube based on the sub-block. Respectively, the eigendirection of the covariance matrix with the largest eigenvalue is orthogonal to $\hat{\Lambda}_0$ as well. Following this eigendirection change from sub-block to sub-block, one maps the magnetic field over wider region of the sky.

The variance of the directions of gradients at individual pixels is determined by the J_2 parameter of the covariance matrix. The J_2 parameter is determined by the properties of the turbulence and the LOS angle of the mean magnetic field. In approximation of Eq. (39) for strong turbulence it is easily calculated to be

$$J_2 \approx \exp(-2(M_A/\sin \gamma)^2) \quad (40)$$

while complete form of the functional dependence of J_2 on M_A and $\sin \gamma$ can be determined by numerically integrating the σ_{ij} components with the power spectrum given in Eq. (38). Fig. 4 shows our result from the numerical calculations as compared to the theoretical expectation in Eq. (40). We can see that the numerical data (from synthetics, blue

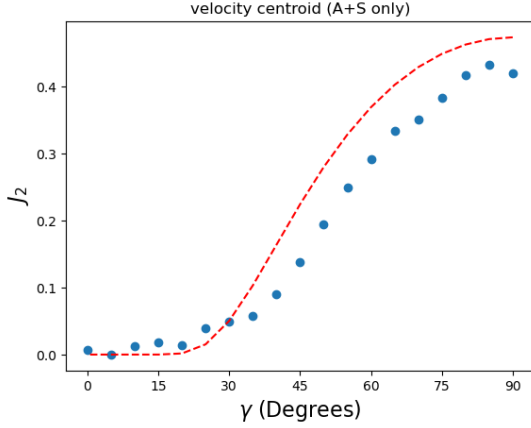


Figure 4. J_2 in centroid maps created from synthetic simulations with equal contributions of Alfvén and Slow modes as a function of γ . The theoretical approximation in Eq. (40) is given by the red dash line. $M_A \approx 0.6$.

points) and the theoretical points (red curve) have very similar trends.

6.4. The susceptibility of our method to noise level

In realistic observations, we will have noise, and the J_2 parameter is naturally smaller since noise introduces more gradient isotropy to the data set. As a result, we would like to evaluate how noise affects our measurement of J_2 in observations. Fig. 5 shows the variation of J_2 of Alfvén mode velocity centroid as a function of the noise-to-signal ratio (N/S) for synthetic and realistic numerical data. To mimic observations, we apply an additional 2-pixel Gaussian smoothing kernel to our data. Again, we have to emphasize that synthetic data demonstrates the effect of beam size and dissipation scales in realistic data. We can see from Fig. 5 that the J_2 parameter indeed decreases dramatically as N/S increases for both synthetic (red points in Fig. 5) and realistic MHD data (blue points in Fig. 5).

7. ESTIMATION OF THE MEAN DIRECTION OF THE FIELD AND ITS VARIANCE ON THE SKY

In the previous sections, we have shown that measurements of the gradients on the sky give information about the local direction of the magnetic field Θ_H and the Alfvén Mach number via the eigen-directions and the anisotropy J_2 of the gradient covariance tensor, respectively. In this section, we analyze the statistical uncertainties if Θ_H and J_2 are determined locally in a $L_p \times L_p$ sub-block. To estimate the errors we assume the Gaussian distribution of the gradients.

7.1. Distribution of the gradient orientations on the sky

In § 5 we have developed a theoretical prediction for the one-point covariance tensor σ_{ij} of the gradient field components. The anisotropy of the gradient map is determined by the J_2 parameter in an invariant coordinate way. At the same time, the two eigen-directions are one aligned and one per-

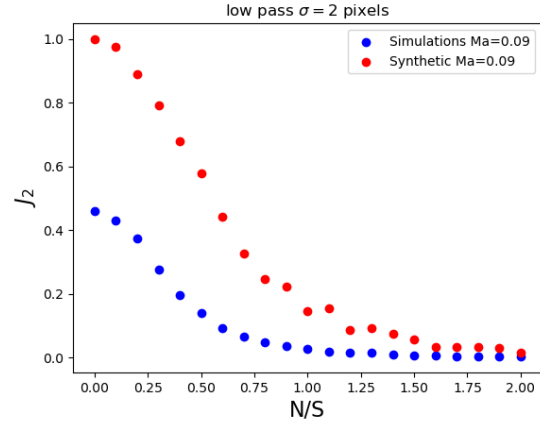


Figure 5. Two figures showing how the introduction of noises changes the measured J_2 in both synthetic (red) and the Alfvén mode fluctuations of simulation data (blue) at $M_A = 0.09$.

pendicular to the local direction of the LOS-averaged magnetic field. Here we present theoretical predictions for more practical statistics in the point of view of variance of the directions of the gradients, that follows from the results of Section 5, assuming that 2D gradients can be described as Gaussian distributed, i.e. in low M_A . Notice that Lu et al. (2020) points out that such assumption of Gaussian distribution on gradient orientation histogram is not correct in the case of low polarization percentage (i.e., $M_{A,LOS}$, the line of sight Alfvén Mach number).

Under Gaussian assumption for gradients, the theoretical expectation of the gradient orientation distribution is given by (Lu et al. 2020):

$$P(\theta) = \frac{1}{\pi} \times \frac{\sqrt{1 - J_2}}{1 - \sqrt{J_2} \cos 2(\theta - \theta_H)} \quad (41)$$

where θ_H is the preferred direction of the distribution that follows the eigen-direction of σ_{ij} with the largest eigenvalue. This preferred direction is orthogonal to the magnetic fields for the turbulence regime that we are considering in this current section. The distribution is defined and normalized over an arbitrary interval of angles with the span of π radians (i.e., $\theta \in [-\pi/2, \pi/2)$). We see the fundamental role the parameter J_2 plays in this distribution: In maximally anisotropic case $J_2 = 1$ the angle distribution given by Equation (41) becomes the Dirac δ_D -function around θ_B with zero variance of orientation. In the opposite limit where the turbulence is isotropic, $J_2 = 0$, i.e. the angle distribution is flat and the *rms* angle deviation $\sigma_\theta = \pi/(2\sqrt{3}) \approx 52^\circ$.

7.2. Statistical uncertainties of the mean field direction and the angle variance from gradients in sub-blocks

Let us first determine the number N of independent and uncorrelated samples of the gradient directions θ_i in a sub-block. We can estimate N from the following considerations. Since gradients are determined by the short wave side of the spectrum, the correlation length L_{corr} between gradients at

neighboring pixels is determined by the largest experimental or synthetic beam scale of the map and the scale of dissipation that damps shortwave perturbations. We can estimate $L_{corr} \approx \max(W_{FWHM}, L_{dis})$ where W_{FWHM} is a full width at half maximum of the beam window. The resulting number of independent measurements in the patch is then

$$N \approx (L_p/L_{corr})^2. \quad (42)$$

7.2.1. Uncertainties of the magnetic field direction Θ_H

The simplest estimator $\tilde{\theta}_H$ of the mean direction of the gradients in a sub-subblock is the average of individual independent measurements

$$\tilde{\theta}_H = \frac{1}{N} \sum_{i=1}^N \theta_i \quad (43)$$

The uncertainty in determining $\tilde{\theta}_H$ is given by variance of the estimator over the whole ensemble of gradient realizations

$$(\Delta\tilde{\theta}_H)^2 \equiv \langle \tilde{\theta}_H^2 \rangle - \langle \tilde{\theta}_H \rangle^2 = \frac{1}{N} \langle (\theta - \theta_H)^2 \rangle \quad (44)$$

To proceed further, let us have the gradient angle distribution described by Eq. (41) in Gaussian assumption for the gradients. With this distribution, the ensemble variance of the angles can be found in terms of special functions, but for simplicity we will approximate it by the ‘‘angle variance’’ Σ^2 , defined as

$$\Sigma^2 \equiv \frac{\langle 1 - \cos 2(\theta - \theta_H) \rangle}{2} = \frac{\sqrt{J_2} + \sqrt{1 - J_2} - 1}{2\sqrt{J_2}} \quad (45)$$

Σ^2 is close to true angle variance $\langle (\theta - \theta_H)^2 \rangle$ if $\theta - \theta_H$ is small. Otherwise, it ranges from zero at zero variance to 1/2 if the distribution of directions is isotropic. The estimated mean direction is then, on average, equal to the ensemble mean with the uncertainty that is suppressed by \sqrt{N}

$$\tilde{\theta}_H = \theta_H \pm \frac{\Sigma}{\sqrt{N}} \quad (46)$$

It is important to note, that as anisotropy level increases with decreasing $M_A/\sin \sigma$ and $\Sigma^2 \rightarrow 0$, the *rms* deviation of the gradient direction decreases only as $\Sigma \sim \sqrt{M_A}/\sin \gamma$, in contrast to *rms* fluctuations of the magnetic field direction itself relative to the mean, which are $\propto M_A$.

7.2.2. Uncertainty of the anisotropy level of the gradients

The information on the M_A is contained in the anisotropy level of the gradient direction distribution, which in turn is determined by the variance of the gradient directions. In line with the previous sections, to treat the periodicity of angles when they are not small, let us consider the quantity $\Sigma_i^2 = \frac{1 - \cos 2(\theta_i - \theta_H)}{2}$ in place of $(\theta_i - \theta_H)^2$.

Then the estimator (designated by tilde) of Σ^2 in a sub-block is

$$\tilde{\Sigma}^2 = \frac{1}{N} \sum_{i=1}^N \Sigma_i^2 \quad (47)$$

The mean value of this estimator is equal to ensemble-averaged Σ^2 given by Eq. (45)

$$\langle \tilde{\Sigma}^2 \rangle = \frac{1}{N} \sum_{i=1}^N \langle \Sigma_i^2 \rangle = \Sigma^2 \quad (48)$$

while the variance of this estimator is

$$\begin{aligned} \langle (\tilde{\Sigma}^2)^2 \rangle - \langle \tilde{\Sigma}^2 \rangle^2 &= \left\langle \left(\frac{1}{N} \sum_{i=1}^N \Sigma_i^2 \right)^2 \right\rangle - \langle \Sigma_i^2 \rangle^2 \\ &= \frac{1}{N} \left(\langle \Sigma_i^4 \rangle - \langle \Sigma_i^2 \rangle^2 \right), \end{aligned} \quad (49)$$

using the presupposition that θ_i are uncorrelated.

With distribution given by Eq. (41) the fourth order cumulant is evaluated to be

$$\langle \Sigma_i^4 \rangle - \langle \Sigma_i^2 \rangle^2 = \frac{J_2 - 1 + \sqrt{1 - J_2}}{4J_2} \quad (50)$$

When angle fluctuations within sub-block are small, $\Sigma_i \approx \theta$, and $J_2 = 1 - \alpha$ with $\alpha \ll 1$, we can use the expansion

$$\langle \Sigma_i^2 \rangle \approx \frac{1}{2} \sqrt{\alpha} \left(1 - \frac{1}{2} \sqrt{\alpha} \right) \quad (51)$$

$$\langle \Sigma_i^4 \rangle - \langle \Sigma_i^2 \rangle^2 \approx \frac{1}{4} \sqrt{\alpha} (1 - \sqrt{\alpha}) \quad (52)$$

Thus we have an estimator $\tilde{\Sigma}^2$ for the angle variance with the mean and uncertainty as follows

$$\langle \tilde{\Sigma}^2 \rangle \approx \frac{1}{2} \sqrt{\alpha} \quad (53)$$

$$\Delta \tilde{\Sigma}^2 = \sqrt{\langle (\tilde{\Sigma}^2)^2 \rangle - \langle \tilde{\Sigma}^2 \rangle^2} \approx \frac{1}{2} \frac{\alpha^{1/4}}{N^{1/2}} \quad (54)$$

The relative uncertainty, therefore, is

$$\frac{\Delta \tilde{\Sigma}^2}{\langle \tilde{\Sigma}^2 \rangle} \approx \frac{1}{\alpha^{1/4} N^{1/2}} \approx \sqrt{\frac{1}{2N\Sigma^2}} \quad (55)$$

which demonstrates that the relative error on angle dispersion increases as angle dispersion becomes smaller (i.e., as the mean direction becomes better determined) but decreases with the increase in the number of independent samples of the gradients in the sub-block.

This is illustrated in Fig. 6 where we plot the J_2 and its error bars as a function of block size L_{block} normalized by the injection scale for both synthetic and real MHD data. We can see that the value of J_2 for both synthetic and real data does not change significantly. However, the numerical data has larger errors for smaller block sizes.

7.3. Relation to projected Mach number

From Eq. (40), J_2 is related to Alfvénic Mach number and the angle between the mean field and the line of sight, $J_2 \approx$

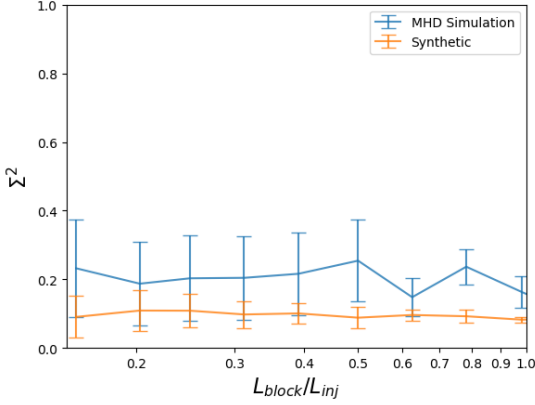


Figure 6. The variation of Σ^2 and its error-bars as a function of block size for Alfvén mode centroid at $\gamma = \pi/2$, $M_A = 0.13$.

$e^{-2M_{A\perp}^2}$, i.e. $\alpha = 2M_{A\perp}^2$, thus $\langle \theta^2 \rangle = \frac{1}{\sqrt{2}} M_{A\perp}$. If $M_{A\perp}$ is determined from the variance of gradient angle Lazarian et al. (2018), the statistical error on this measurement is

$$\frac{\Delta M_{A\perp}}{M_{A\perp}} = \sqrt{\frac{1}{\sqrt{2} M_{A\perp} N}} \quad (56)$$

For instance, for $M_{A\perp} = 0.1$, the statistical error is 10% if we have $N = 1000$ uncorrelated samples of a gradient in the patch (oversampling of a smoothing scale will not decrease the error). We must remember, of course, that the expansion part of our analysis is valid only when $M_{A\perp} = M_A / \sin \gamma \ll 1$, which will not hold for too small γ .

In Fig. 7, we present theoretical curves for Σ as functions of $M_A / \sin \gamma$ while varying the mean direction of the magnetic field within the local patch relative to the LOS. We consider two cases of observables, namely gradients of velocity centroids and synchrotron intensity, and two models of turbulence. purely Alfvénic turbulence, and strong turbulence in high- β regime with equal contribution of Alfvén and slow modes. Remarkably, in all these cases, the universal approximation $J_2 \approx \exp(-2(M_A / \sin \gamma)^2)$ is excellent. One observes that for Alfvénic turbulence, there is more sensitivity to the mean field angle γ in the regime of $M_A / \sin \gamma > 0.5$, with the fit performing best for small γ where magnetic field is more along LOS. At the same time, for more perpendicular orientation, it is actually the linear expansion of the fit $J_2 \sim 1 - 2(M_A / \sin \gamma)^2$ that gives a better match up to $M_A / \sin \gamma < 0.6$, i.e., until the angle variance starts reaching its saturation level at $\Sigma = 1/\sqrt{2}$.

8. APPLICATION OF GRADIENT THEORY TO OBSERVABLES OF MHD TURBULENCE

8.1. Alternative measures available from observations

We have developed our theory in terms of J_2 , Eq. (22), which can be obtained from observations by estimating the covariance tensor of the gradients in the sky patch. However, one can measure the anisotropy of the gradient orientations using quantities which, although mathematically related to

J_2 , may have own advantages in convenience of the measurement or properties of the uncertainties. They are particularly useful in the regime of high anisotropy, when J_2 is nearly saturated close to unity, $J_2 \approx 1 - 2(M_A / \sin \gamma)^2$. We will not study this estimators in detail here, but just enumerate some popular choices and their behavior for sub-Alfvénic regime

1. The “angle variance” Σ^2 , defined as

$$\Sigma^2 \equiv \frac{\langle 1 - \cos 2(\theta - \theta_B) \rangle}{2} = \frac{\sqrt{J_2} + \sqrt{1 - J_2} - 1}{2\sqrt{J_2}} \quad (57)$$

$$\Sigma^2 \approx (1/\sqrt{2})(M_A / \sin \gamma), \quad M_A / \sin \gamma < 1$$

Σ^2 is close to true angle variance $\langle (\theta - \theta_B)^2 \rangle$ if $\theta - \theta_B$ is small. Otherwise, it ranges from zero at zero variance to 1/2 if the distribution of directions is isotropic. Determining Σ^2 requires preliminary determination of the mean direction in the patch, around which the fluctuations are measured.

2. The p^2 function, which is similar to degree of polarization in polarization studies,

$$p^2 \equiv \langle \cos 2\theta \rangle^2 + \langle \sin 2\theta \rangle^2 = \frac{(1 - \sqrt{1 - J_2})^2}{J_2} \quad (58)$$

or, its reciprocal $V = 1 - p^2$ with the range from zero (zero variance, i.e. maximal anisotropy) to one (isotropic):

$$V \equiv 1 - p^2 = 2 \times \frac{J_2 + \sqrt{1 - J_2} - 1}{J_2} \quad (59)$$

$$V \approx 2\sqrt{2}(M_A / \sin \gamma), \quad M_A / \sin \gamma < 1$$

3. The “bottom to top ratio” B/T that we define as the ratio of peak to the lowest value of the distribution function

$$\frac{B}{T} \equiv \frac{P(\theta = \theta_B + \pi/2)}{P(\theta = \theta_B)} = \frac{1 - \sqrt{J_2}}{1 + \sqrt{J_2}} \quad (60)$$

$$\frac{B}{T} \approx (1/2)(M_A / \sin \gamma)^2, \quad M_A / \sin \gamma < 1$$

B/T ranges from zero at zero variance to one if distribution is isotropic. Lazarian et al. (2018) presented empirical dependencies between the dispersion of the velocity gradient orientation and inverse T/B (top-to-bottom) ratio with the local plane of sky Alfvénic Mach number $M_{A,\perp}$. Employing this technique it was possible (Hu et al. 2019d) to estimate the magnetization of a number of molecular clouds on the sky and obtain previously unavailable magnetic information on a high velocity cloud hid behind the galactic arm.

In conclusion, we see that all measures of angle variances of the gradients of any single is determined by a single parameter J_2 , which in turn is given by the quadrupole to monopole ratio of 2D on-sky structure function of the signal at zero separation.

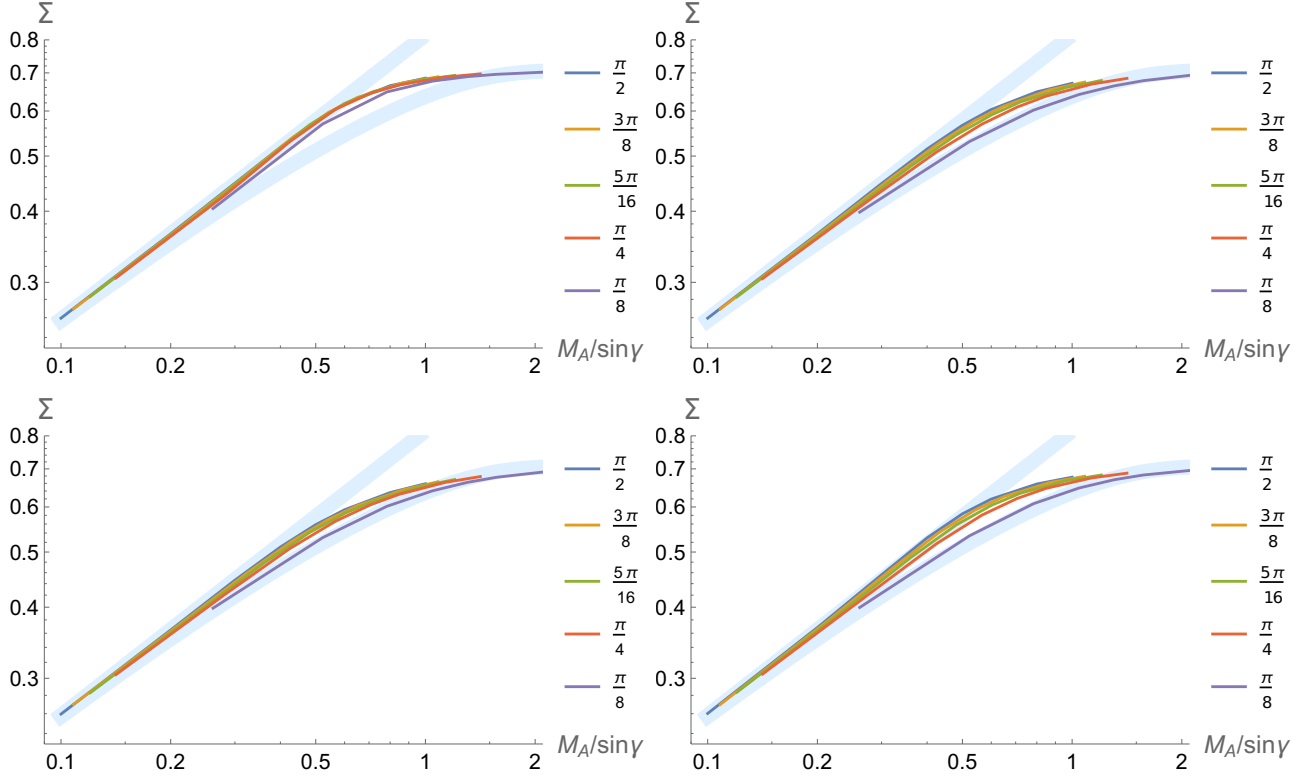


Figure 7. Σ parameter for velocity centroids (top row) and synchrotron intensity gradients (bottom row) in strong (left column) and Alfvénic (right column) turbulence. The functions are plotted versus perpendicular $M_{A\perp} = M_A / \sin \gamma$ argument, for several angles γ between the mean magnetic field and the line of sight, as labeled. Curved thick light blue line corresponds to approximation $J_2 = \exp(-2M_A^2 / \sin^2 \gamma)$, while straight thick blue line is its expansion $J_2 \approx 1 - 2M_A^2 / \sin^2 \gamma$

8.2. Gradients of Centroids

Velocity Centroid presents the most straightforward case on our application of Eq. (40) as there is no extra caution that we have to take care of as long as density contributions are removed properly (Yuen et al. 2021). The projection of *Alfvén mode* velocities follows the formalism of Eq. (39) without any doubt. In this subsection, we will discuss how different modes enter Eq. (40). For simplifications, since MHD theory predicts that the slow modes follow pretty much similar scaling as the Alfvén mode (see, e.g. Lazarian & Pogosyan 2004), therefore we will limit our discussion to turbulent media with admixtures of Alfvén and fast modes only.

In Fig. 8 we show how our four observables discussed in §7 derived from the Alfvén mode synthetic simulations are varied as a function of M_A . We plot the variations of these observables against the theoretical expectations that we did in §7. We can see that in the case of pure Alfvén modes, the synthetic data points follow the theoretical expectations very nicely.

Furthermore, we show in Fig. (9) on how the four parameters that we described in the current section vary as a function of M_A in synthetic centroid maps from realistic numerical simulations with all non-Alfvén mode filtered out and with $M_A < 1$ and $M_s > 1$. This is the condition where most molecular clouds are residing. To compare with the theo-

retical prediction, we plot the exact theoretical expectations following Eq. (40). We can see that the numerical result (blue points in Fig. 9) follows a very similar trend to the theoretical expectation.

8.3. Gradients of Synchrotron Intensity

For completeness, we would also like to discuss how J_2 varies if we consider the gradients of synchrotron intensity (Lazarian et al. 2017). One particular difference between the gradients of centroid and the gradients of synchrotron intensities is that the former is a linear projection of the *line of sight* velocity fluctuations. At the same time, the latter is the quadratic projection on the plane of sky components. The tensor factor (see LP12) is crucial in explaining the orientations of the gradients for the compressible modes. However, for the case of Alfvén modes, the crucial factor is still the anisotropy factor we discussed in §5. We therefore expect the J_2 factor for synchrotron intensities to follow similarly to that of centroid.

To verify our idea, we perform the same 4-parameter test as in Fig. 8 by replacing the velocity centroid to synchrotron intensity maps from synthetic simulations. The results are shown in Fig. 10. We can see from this figure that all four parameters follow the theoretical expectations rather nicely, similar to that of the centroid.

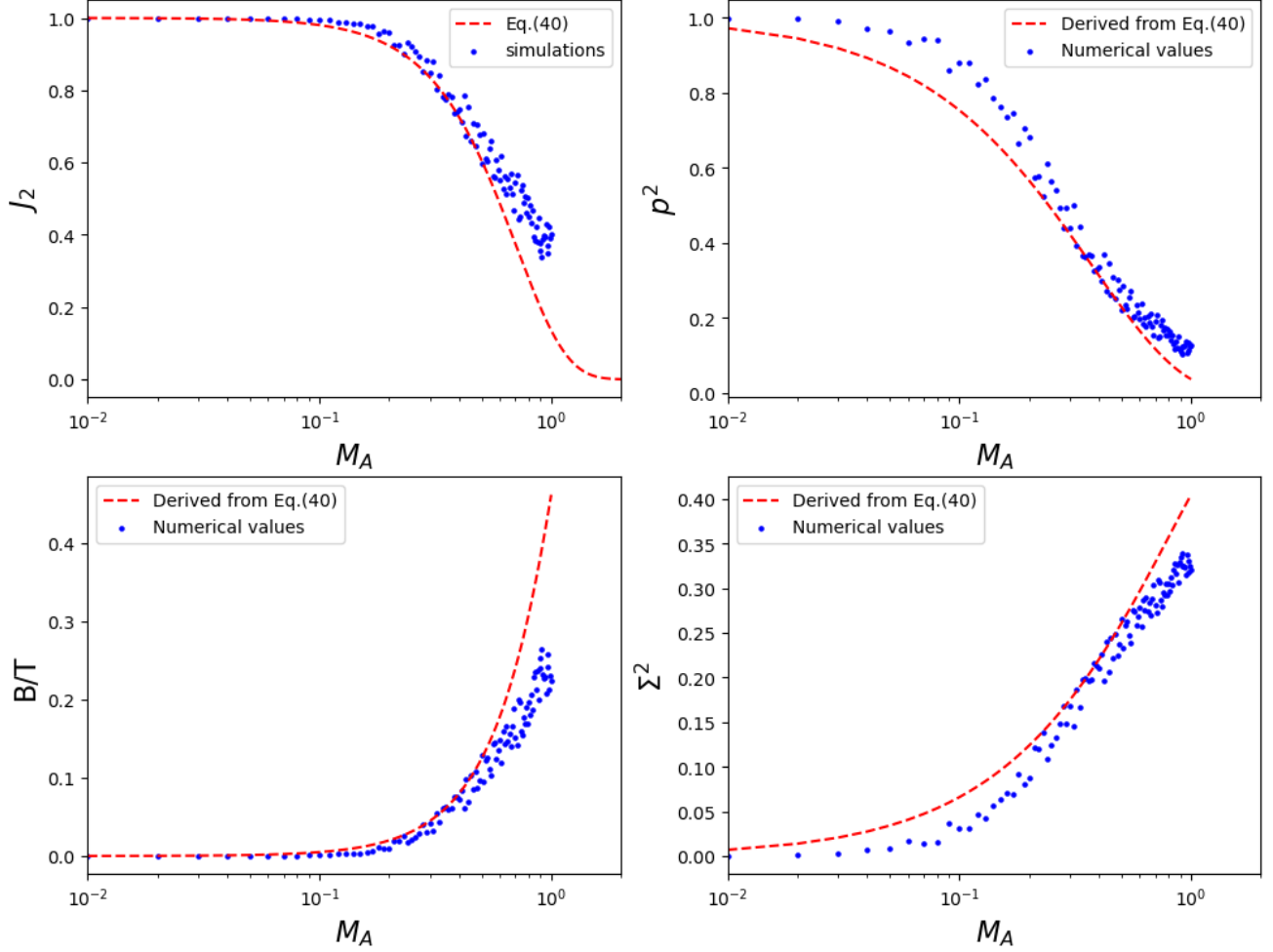


Figure 8. A figure comparing the theoretical expectation (red) to data points from synthetic simulations for velocity centroids with pure Alfvén modes for all four observables as a function of M_A . From top left: J_2 , p^2 , B/T and Σ^2 .

8.4. Variation of the J_2 - M_A relation in numerical data

From Figs. 8–10, we observe a deviation between theory and observation even in the case of pure Alfvénic modes. It could be questioned whether approximations, in particular a sample form of the power spectrum Eq. (38) that led to Eq. (40) are statistically accurate enough. To quantify the deviation between the analytical J_2 given by approximation of Eq. (40) and numerics (both from synthetic models based on Eq. (36) and actual MHD simulations), let us assume that the actual relation between J_2 and M_A can be parameterized as:

$$J_2 = \exp(-CM_A^n) \quad (61)$$

for some constants C and n . On the top panel of Fig. 11, we plot the J_2 value from analytical (red dash line), synthetic (green dots), and MHD simulation data (blue dots) as a function of M_A . While theoretical approximation falls faster than synthetic and MHD simulations as M_A approaches unity, both data resemble the analytical model of Eq. (40).

To quantify statistical correspondence further, we generate 100 samples of synthetic cubes at $M_A = 0.1$ using Eq. (27)

and then perform an MCMC (Monte-Carlo Markov Chain) calculation on the synthetic data, assuming that Eq. (61) applies. Each synthetic data cube gives a pair of values of C , n . The bottom panel of Fig. 11 shows the distribution of n from the MCMC experiment, in which we select the number of bins to be the square root of the sample size (namely 10) to satisfy the statistical criterion. The peak of the distribution is roughly at ~ 2 , which is consistent with Eq. (40). The dispersion of the values of n is ~ 0.4 , which provides an estimation of the accuracy of Eq. (40) when applying to observations.

9. ADVANCES OF THEORY AND NEW OPPORTUNITIES

9.1. The “kinematic” Alfvénic Mach number under different driving cases

Earlier in the paper, we focused on the Alfvénic component of the MHD turbulence cascade. This treatment is feasible due to the relative independence of the Alfvénic motions from the influence of other types of MHD fluctuations and the dominance of Alfvénic fluctuations in determining the gradient properties. For some other applications, we must

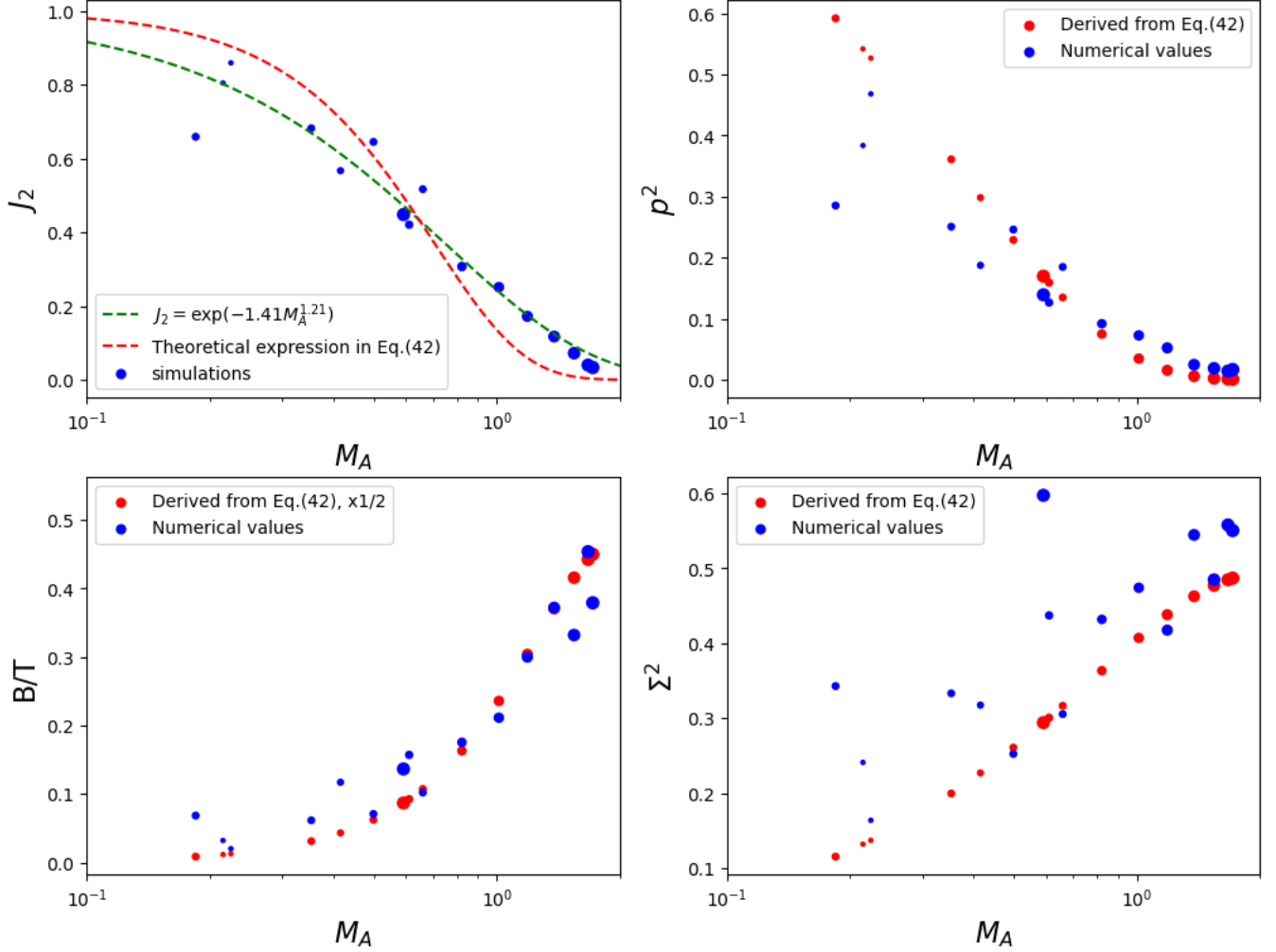


Figure 9. Four panels showing our theoretical prediction (Eq.40) and its derivatives, (red) relative to the actual numerical results (blue). For J_2 we fit the numerical results with $\exp(-CM_A^n)$ with the green curve.

consider non-Alfvénic types of turbulent motion. In this situation, the magnetic and velocity fluctuations are not connected through the Alfvén relation, and the total injection velocity δv_L is larger than the V_{inj} that initiates the Alfvénic cascade.

The considerations above mean that the ratio of $\delta v_L/V_A$ is larger than the Alfvén Mach number defined by Eq. (6), and this ratio defines another quantity, which we will term “kinetic” Mach number:

$$M_{A,k} \equiv \frac{\delta v_L}{V_A}, \quad (62)$$

A recent study in Lazarian et al. (2023) of sub-Alfvénic turbulence in incompressible limit revealed that the relation between $M_{A,k}$ and M_A depends on whether the turbulence was driven by velocity or magnetic perturbation. In the former case, velocity components *parallel to the mean field* at the injection scale increase the kinetic energy of turbulent motions compared to the case of magnetic driving. The physical effect is the natural consequence of fluid fluctuations

along stochastic but stiff magnetic field lines. In the case of velocity-driven incompressible MHD turbulence, Lazarian et al. (2023) derived that

$$\mathcal{E}_b \approx M_A^2 \mathcal{E}_k, \quad (63)$$

where \mathcal{E}_b is the energy of magnetic turbulence and \mathcal{E}_k is the kinetic turbulent energy. Therefore,

$$M_A = M_{A,k}^2. \quad (64)$$

Relations similar to Eqs. (63) and (64) were empirically obtained in Beattie et al. (2022) using MHD compressible simulations, which suggests that the compressibility does not substantially alter the corresponding physics.⁸ Thus, we expect these relations to hold approximately for various astrophysical conditions.

⁸ In Beattie et al. (2022) these expressions were interpreted as the consequence of the compressibility effects.

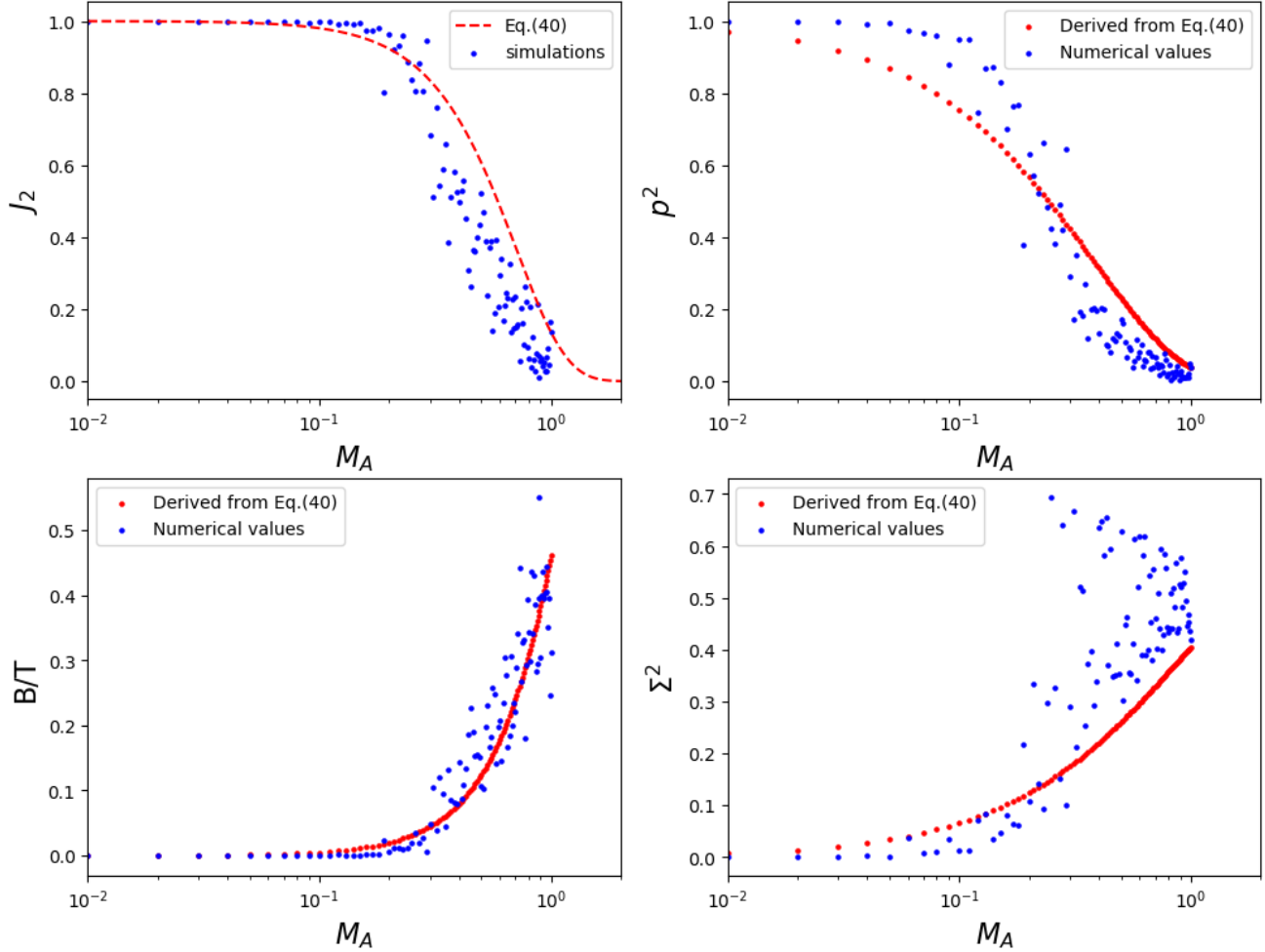


Figure 10. Similar to Eq.8 but with synchrotron intensity gradients. From top left : J_2 , p^2 , B/T and Σ^2 .

If magnetic fluctuations drive the turbulence, Lazarian et al. (2023) also showed that $M_{A,k} = M_A$. The paper outlined a procedure for distinguishing the magnetically and velocity-driven turbulence. In many astrophysical settings, we expect the turbulence to be driven by velocity injection.

The equations for sub-Alfvénic turbulence in LV99 and subsequent studies (e.g., LP12, Lazarian & Pogosyan 2016) assumed that the fluctuations at the injection scale are Alfvénic, i.e., that the $M_A = M_{A,k}$ as in Eq. (6).

9.2. New technique in obtaining magnetic field strength independent of polarimetry: The MM2 approach

Consider first the idealized setting with pure Alfvénic turbulence observed perpendicular to the mean magnetic field. In this case of magnetic driving of turbulence, the magnetic field fluctuation $\delta\phi$ is directly related to the velocity Alfvén Mach number:

$$\delta\phi \approx M_A \quad (65)$$

Thus, the classical Davis-Chandrasekhar-Fermi (DCF) expression (Davis 1951; Chandrasekhar & Fermi 1953) for determining magnetic field from observations can be rewritten

as

$$B_0 \approx \sqrt{4\pi\rho} \delta v M_A^{-1}. \quad (66)$$

Astrophysical turbulence is a mixture of 3 cascades, fast, slow, and Alfvén modes⁹, rather than pure Alfvénic turbulence (Cho & Lazarian 2002, 2003). Accounting for different modes was done using the alternative technique of magnetic field strength study, differential measurement analysis (DMA), which can measure the distribution of magnetic field intensity (Lazarian et al. 2021). However, in this paper, we limit ourselves to the constraints of the traditional DCF, where no decomposition into modes is employed.

Let us now eliminate the turbulent velocity term δv using the expression of sonic Mach number $M_s = \delta v/c_s$, where c_s is the sound speed, obtaining instead of Eq. (66)

$$B_0 \approx c_s \sqrt{4\pi\rho} M_s M_A^{-1}, \quad (67)$$

⁹ We use the term “modes” rather than “waves”, since in turbulence, the non-linear interactions are essential. These interactions make Alfvén and slow modes decay within one period.

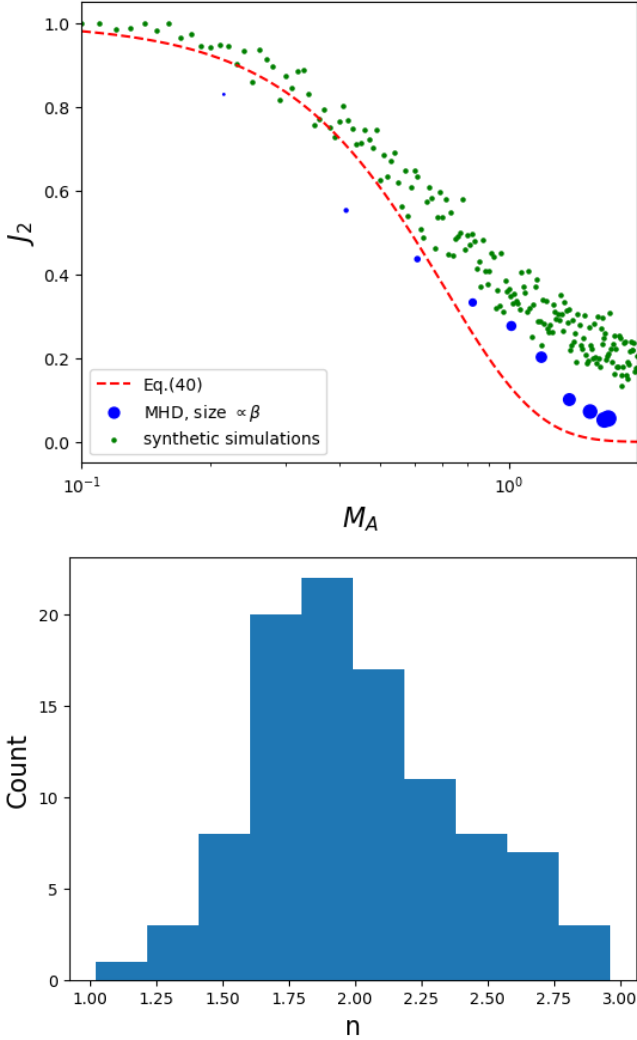


Figure 11. (Top) A figure showing how the J_2 parameter computed from both synthetic (green points) and MHD (blue points) simulations are compared to the theoretical prediction in Eq. (40), red dashed line). (Bottom) The Monte Carlo results in estimating the fit on synthetic data on the formula $J_2 = \exp(-CM^n)$, showing the mean value of n to be ~ 2 .

which is the expression obtained in Lazarian et al. (2020) within the approach termed there MM2 to denote the employment of two Mach numbers.

Our present study shows that gradient distribution directly measures from observations $M_{A,mes} = M_A / \sin \gamma$. Using this measure, in case of magnetic driving, one can rewrite Eq. (67) as

$$B_{\perp} \approx c_s \sqrt{4\pi\rho} M_s M_{A,mes}^{-1}, \quad (68)$$

where B_{\perp} is the plane of the sky magnetic field component. Eq. (68) can be used to find the perpendicular component of magnetic field for both velocity and magnetic field driving.

At first glance, nothing major has been achieved by substituting M_s instead of δv . However, it is important to realize that M_s can be measured differently. Focusing on gradients,

M_s can be obtained in spectroscopic channel maps measuring the amplitudes of gradients (Yuen & Lazarian 2020a). This way of measuring magnetic field strength was used to obtain the 3D distribution of magnetic field strengths in the Milky Way using HI data, as demonstrated in Hu & Lazarian (2023a).

For another example, Burkhardt et al. (2009) showed that M_s can be obtained by measuring the kurtosis and skewness of the PDFs of the intensity fluctuations within the channel maps. This is important as in the galaxy, a significant line broadening arises from regular motions, e.g., differential rotation, not related to turbulence. The separation of the turbulent and regular motions may be difficult or even not possible. At the same time, the regular differential motion can distinguish the contribution along the line of sight, providing the 3D information.

An approach similar to the one of Burkhardt et al. (2009) was employed for maps of synchrotron polarization gradients¹⁰ in Gaensler et al. (2011) and Burkhardt et al. (2012) also to constrain M_s . In the latter case, there is no linewidth information, but one can still obtain the value of M_s .

Other ways of obtaining M_s from observational data include using the Tsallis statistics (Esquivel & Lazarian 2005, 2010), genus (Chepurnov et al. 2008), with ongoing research opening up new possibilities for M_s determination. Therefore, the MM2 approach utilizing two Mach numbers in Eq. (67) provides yet another promising way of measuring the magnetic field strength.

As discussed in §9.1, there are additional degrees of freedom depending on whether the turbulence is driven through magnetic or velocity fluctuations at the injection scale. As shown in Lazarian et al. (2024), one can write a universal relation for magnetic field strength

$$B_0 \approx \sqrt{4\pi\rho} \delta v M_{A,k}^{-1}, \quad (69)$$

where the "kinetic Alfvén Mach" number is employed. DCF Eq. (66) comes from equating $M_{A,k}$ to $M_A = \frac{\delta B}{B}$, and obtaining the latter from polarization angle distribution. This is valid in case of magnetic driving. In the case of velocity driving, the "kinetic Alfvén Mach number" $M_{A,k}$ can be determined from M_A via Eq. (64) and the traditional DCF expression is modified¹¹ to

$$B_0 \approx \sqrt{4\pi\rho} \delta v M_A^{-1/2}. \quad (70)$$

Thus, if we deal with the case of velocity driving, Eq. (64) should be used to relate $M_{A,k}$ to $M_{A,mes}$. The possibility of observationally determining the type of driving was discussed in Lazarian et al. (2023).

9.3. MM2 with different types of gradients

¹⁰ These papers did not identify these gradients as the way of magnetic field studies. The latter step was done in Lazarian & Yuen (2018a).

¹¹ The empirical modification of this type was first suggested in Skalidis & Tassis (2021).

Our present analytical study directly addresses two types of gradients: gradients of velocity centroids and gradients of synchrotron intensities. The extension of the theory to other types of gradients is straightforward, but is beyond the scope of our paper. The availability of analytical theory is very synergetic to our earlier attempts to gauge the properties of gradients, e.g. the relation between the statistics of gradients to the media magnetization, with numerical simulations in Lazarian et al. (2018). Both the analytical theory and the aforementioned gauging can be applied to a variety of data set within the MM2 approach. Several selected benefits of this are listed below.

The Synchrotron Intensity Gradients (SIGs) (Lazarian et al. 2017) demonstrate the ability to trace the magnetic field using just the information of synchrotron intensities. Using the latter, the conventional way of obtaining the magnetic field strength is to assume the equipartition of cosmic rays and magnetic field energies. This is a very uncertain assumption, and there are many reasons why it can be violated (Seta et al. 2018). Obtaining the magnetic field with the MM2 removes this assumption and provides a unique way to explore the balance between the magnetic field and cosmic rays.

The Synchrotron Polarization Gradients (SPGs) (Lazarian & Yuen 2018a) provide significant advantages compared to tracking magnetic fields with polarization directions. For instance, using the polarization measurements, the direction of the magnetic field can be obtained only after correcting for the Faraday rotation. Suppose the polarized radiation comes from an external source with no intrinsic Faraday rotation. In that case, the Faraday rotation can be accounted for using multiple polarization measurements at different wavelengths (see Beck 2015). However, if the same volume is responsible for both the synchrotron emission and Faraday rotation, restoring the line of sight averaged magnetic field is impossible, even with multi-frequency polarization measurements. At the same time, the SPGs provide the ability to establish the POS magnetic field direction with the polarization data taken at a single frequency.¹² If, however, multi-frequency polarization measurements are available, the SPGs provide a way of restoring the 3D structure of a magnetic field, as was demonstrated in Lazarian & Yuen (2018c) and Ho et al. (2019). As a bonus, by comparing the intensity of polarized radiation with the results obtained with MM2, one can estimate the 3D variations of the ratio of the magnetic field to the cosmic ray energies.

The particular advantages of applying the MM2 approach to different data sets include

- for synchrotron intensity data, it is possible to decouple the contributions of magnetic field intensity and the relativistic electrons.

- for Faraday rotation data, it is possible to obtain the strength of the POS component of the magnetic field and decoupling the contribution of thermal electrons and a parallel component of the magnetic field to the rotation measures.
- for synchrotron polarization multifrequency data, it is possible to provide the 3D tomography of magnetic field strength

The combination of the first 2 items allows to explore variations of POS magnetic field in different phases of multiphase media along the line of sight. This is synergetic with the input from item 3 in the list.

10. DISCUSSION

10.1. Theoretical understanding of gradients

The first major advance of our study above is the analytical descriptions of gradients. The foundations of the GT are rooted in the theory of MHD turbulence and turbulent reconnection (GS95; LV99) as well as in the analytical description of the statistics of the turbulence parameters available from observations (Lazarian & Pogosyan 2000, 2004, 2006, 2008, 2012, 2016; Kandel et al. 2016, 2017a). The GT has already been proven to be a powerful way of tracing magnetic fields (see Yuen & Lazarian 2017a,b; Lazarian & Yuen 2018b,a; Lazarian et al. 2018; Hu et al. 2021; Hu & Lazarian 2023a). The analytical theory formulated in this paper provides the solid foundations and justifications for the empirical procedures employed within the technique. It opens avenues for new approaches that increase the reliability of the gradient technique. For instance, the formulated theory allows us to understand how the distribution of the gradients over the sub-block used for obtaining individual gradient "vectors" depends on the media magnetization. Indeed, while an earlier study Lazarian et al. (2018) empirically finds that the gradient dispersion has a power law relation to M_A , the power law index was not physically justified. In contrast, the present paper provides analytical predictions for the measures of gradient anisotropy (c.f. Eqs. (40,45,59,60)) that are available from observations.

Our present study deals with Alfvén and slow mode fluctuations of sub-Alfvénic at scales less than LM_A^2 , at which a strong MHD turbulence model is applicable. The anisotropy related to fast modes is significantly weaker compared to Alfvén modes, and fast modes' contribution is frequently subdominant in terms of energy. Thus, we do not consider the effect of fast modes within our present study.

Compared to Lazarian et al. (2018), our study extends the choice of measures that can be used to describe media magnetization. The ratio F of the quadrupole D_2 and the monopole D_0 moments (see Eq. (23)) was calculated in LP12 for synchrotron intensity fluctuations and was generalized for in KLP16 and KLP17, respectively, for the intensity fluctuations in channel maps and velocity centroids. This ratio is directly related to the value of J_2 given by Eq. (22) and is directly related to the measures available with gradients (see Eqs. (45), (58), (60)). Our study demonstrates that

¹² We note that the polarization data may not sample the entire volume due to the Faraday depolarization effect. Thus, the magnetic field obtained with SIGs and single-frequency SPG measurement may differ. This difference carries the information about the depolarization.

different measures can have different advantages for practical applications. For instance, it is possible to show that for sufficiently small M_A , e.g., less than 0.3, the changes of F and J_2 are very weak with the change of M_A . At the same time, for this range of M_A , the differences in measures given by Eqs. (45), (58), (60) is easier to detect.

Finally, the GT theory predicts differences in how gradients and polarization are summed up along the line of sight. In the presence of regular and random magnetic field components, the fluctuations in the polarization Stokes parameters add up in the random walk manner. In contrast, the regular magnetic field contribution increases linearly. As a result, the observed amplitude of the variations of the polarization direction decreases if the line of sight extension of the region exceeds the turbulence injection scale. In contrast, this effect is absent for the gradient magnetic field mapping. This difference stems from the fact that the regular field does not induce gradients. This is expected to induce a systematic difference between the magnetic field direction obtained with gradients and dust polarization using gradients (Lu et al. 2020; Hu et al. 2020b). The analytical description of the gradients opens ways to quantitatively account for this difference.

10.2. 3D distribution of magnetic field strength

The second advance achieved in the present study is the description of how gradients can provide magnetic field strength, i.e., the advancement of the MM2 technique. One of the important applications of this technique is mapping the 3D distribution of the galactic magnetic field vectors. This approach employs the galactic rotation curve as demonstrated in Hu & Lazarian (2023a). The mapping from the velocity space to the galactic coordinate is determined up to the turbulent velocity dispersion. The corresponding $\delta v \sim v_{turb}$ is the coarse grading for the line of sight V_z to z mapping. In terms of molecular clouds, the galactic rotation curve opens ways of studying magnetic fields of molecular clouds in the galactic disk, i.e., the clouds for which crowding along the line of sight prevents magnetic field studies using traditional polarimetry.

The variety of species that can be used for studying magnetic fields by spectroscopic means must provide a complementary way of exploring the 3D magnetic field distribution. For instance, Hu et al. (2019c) demonstrated that the magnetic field direction and M_A can be traced at different distances from the molecular cloud surface using the emission of different molecular species that form at different optical depths. A similar approach is possible for finding M_s (Yuen & Lazarian 2020a). Different species, molecules, and various ions can be employed to test the magnetic field in the ionized part of the ISM.

Measuring magnetic field with gradients using synchrotron intensity and synchrotron polarised intensity of Faraday measure input (see §9.3) provides additional synergy for the 3D magnetic field studies. For instance, synchrotron radiation from SIGs and SPGs mainly test magnetic fields in the hot and warm phases of the ISM at high latitudes (see the description of idealized ISM phases in Draine (2009)), while

Faraday rotation is biased to probing magnetic fields in the regions with higher thermal electron densities, e.g., HII regions. In addition, as described in Lazarian & Yuen (2018b), measuring SPGs at different frequencies makes it possible to sample magnetic fields at different depths from the observer (see also Ho et al. (2019)).

The MM2 approach can be applied to other non-spectroscopic data sets. For instance, the Intensity Gradients (IGs) (Lazarian & Yuen 2018b; Hu et al. 2019b) deal with the column density data that is also affected by MHD turbulence. They can be used with emission lines without the required spectroscopic resolution. Due to the good coupling of interstellar gas and dust, they can also be used with the Far Infrared dust emission data. The IGs reflect the properties of density fluctuations in turbulent media. Those deviate significantly from the underlying turbulent velocity field in the case of supersonic MHD turbulence (see Beresnyak et al. 2005; Kowal et al. 2007). In this case, as first demonstrated by Yuen & Lazarian (2017a), the IGs can trace interstellar shocks. This makes IGs an auxiliary source of information for restoring magnetic field direction and obtaining M_A in combination with velocity gradients. For subsonic turbulence, IGs can be directly used to study magnetic fields within the MM2 approach.

The advances in the analytical description of turbulent statistics make the gradient approach more versatile. In KLP18, it was shown that in the presence of dust absorption, the sampling of turbulence in the media is limited by the surface layer, the thickness of which is determined by the dust absorption. As this absorption is wavelength-dependent, it provides a way to sample deeper into the cloud using a longer wavelength. The ability to sample magnetic fields on the surface of the clouds using optical emission lines presents an advantage in itself.

10.3. Gradients and polarization studies: advantages and synergy

Polarization and gradient measurements present two major ways of probing POS magnetic fields. The present study illustrates the differences and the synergy of the two approaches.

Measurement of magnetic fields with gradients and polarization are similar because both trace the direction of the local magnetic field, and neither measure is sensitive to the amplitude of the magnetic field. Casting the gradient measure in terms of pseudo-Stokes parameters accumulated along the LOS (Lu et al. 2020) highlights the formal similarity. However, there are two important differences. First is that polarization directly reflects the mean magnetic field as well as its fluctuations. Whereas the gradients are not sensitive to constant field being directly affected only by the variable part of the field, so that the mean magnetic field direction is found from gradients only statistically. Second difference is that polarization has a long correlation scale across the sky, similar to magnetic field, while the correlation length of the gradients is much shorter.

These differences affect the determination of M_A from the data. The way of measuring M_A with gradients was first explored in Lazarian et al. (2018) and has shown several advantages compared to the corresponding measurements of M_A using polarization. The most notable is that gradient measurement of M_A can be achieved within an individual sub-block. Local determination of M_A from polarization angles is hampered by the presence of long correlations that requires sky coverage exceeding L_{inj} to evaluate the full variance of the angles. Thus, applying the GT returns a spatial distribution of magnetization rather than a single value of M_A from measuring dust polarization.

Additionally, the presence of both regular and random magnetic fields along the line-of-sight decreases the dispersion of polarization angle $\delta\phi \sim \frac{\int_{\mathcal{L}} \delta B_{\perp} dz}{B_{\perp} \mathcal{L}}$ by a factor $\sqrt{L_{inj}/\mathcal{L}}$ if the thickness of the turbulent cloud along the line of sight \mathcal{L} is larger than the turbulent injections scale L_{inj} . On one hand this improves the accuracy with which mean field direction is determined by polarization. On the other hand, this effect is not easy to quantify when analyzing the polarization angle variance, and it can significantly distort the value of M_A obtained with the polarization measurements. On the contrary, the theory presented in this paper demonstrates that the gradients can return the true value of M_A . A comparison of the dispersion of the polarization and M_A obtained with gradients can provide an estimate of L_{inj}/\mathcal{L} , which can be used to determine the turbulence injection scale L_{inj} .

Compared to dust polarization, the gradient advantage is that they are unaffected by grain alignment efficiency variations and alignment direction variations that can be induced by strong radiation (Lazarian & Hoang 2007; Andersson et al. 2015b). However, the outflows and gravitational collapse can switch the direction of gradients from the default perpendicular to the magnetic field to parallel to the field (Hu et al. 2020a; Hu & Lazarian 2023b). The synergetic combination of polarization and gradients opens ways to decrease the uncertainties relevant to both techniques and get a unique insight into the underlying physical processes.

A serious advantage of gradients compared to synchrotron polarization is that the gradients are unaffected by the Faraday rotation/depolarization (Beck 2015). By combining the gradients and synchrotron polarization, one can also get the Faraday rotation measure and, therefore, an estimate of the magnetic field component parallel to the line of sight B_{\parallel} without involving troublesome multi-frequency measurements. In addition, by applying a gradient approach to different measures obtained from synchrotron polarization (Lazarian et al. 2017; Zhang et al. 2019, 2020b), one can reconstruct the magnetic field distribution in 3D space (Ho et al. 2019).

The synergetic use of gradients and polarization is also possible for the CMB studies. The polarization gradients arising from the synchrotron foreground are aligned parallel to the foreground polarization. The polarization of cosmological origin is not expected to have this property. This can help solve the important problem of distinguishing the polarization of cosmological origin from foreground polarization.

11. CONCLUSIONS

This paper presents the theory of the Gradient Technique, which applies to different types of gradients originating in turbulent MHD flows. Our study applies the theory to gradients of velocity centroids and synchrotron intensities. However, this approach can be generalized to Velocity Channel Gradients (VChGs), Synchrotron Polarization Gradients (SPGs), Faraday Rotation Gradients (FRGs), etc.

The universality of the theory stems from the small size of the adopted sub-blocks of data averaging compared to the turbulence injection scale. In this setting, the effect of the correlations of the gradients along the line of sight is negligible, and the dispersion of gradients along the line of sight is determined by the dispersion of magnetic field directions on the injection scale rather than the statistics of emission that we employ to measure the gradients. The MHD turbulence cascade's Alfvénic component determines the latter dispersion. The dispersion changes only marginally with the extent of the line of sight L if $L > L_{inj}$. This is very different from the dispersion of the polarization "vectors," for which the dispersion gets narrow as L gets larger compared to L_{inj} .

The theory testifies that the properties of the distribution of gradients reflect the distribution of the POS component of magnetic field for $M_A/\sin\gamma < 1$, where γ is the angle between the line of sight and the mean magnetic field. The deviations increase when the aforementioned ratio gets larger than unity as the fluctuating magnetic field gets larger than the POS component of the mean magnetic field.

The observed gradient directions are dominated by the largest spacial frequencies of the image, with the gradients calculated on the smallest resolved scales dominating the resulting directions. The smallest eddies in MHD turbulence closely follow the direction of the magnetic field in their vicinity. Therefore, similar to the polarization from aligned dust, the gradients can provide the image of the magnetic field projected along the line of sight.

In terms of practical tracing of magnetic fields and the distribution of magnetization, the theory demonstrates that

- It is possible to obtain the detailed distribution of the media magnetization.
- The obtained magnetization value is robust and changes only marginally with the length of the line of sight L when $L \gg L_{inj}$.

In addition, in the paper, we explored a new way of probing the strength of POS magnetic field by using the ratio of sonic and Alfvén Mach numbers, i.e., M_s and $M_{A,\perp}$. This technique can be applied to various data sets, including spectroscopic data, synchrotron intensity, polarization data, etc. When applied to spectroscopic data, MM2 provides

- a detailed distribution of the plane of sky magnetic field strength;
- 3D distribution of plane of sky magnetic field galactic disk magnetic fields, if galactic rotation curve is employed;

- the 3D distribution B_{\perp} strength in molecular clouds if a combination of emission lines from molecular species formed at different optical depths is used.

Our study of extending the MM2 technique for studying magnetic field strength using synchrotron intensity, synchrotron polarization gradients, and gradients, as well as density gradients.

Acknowledgments. We cordially thank Jungyeon Cho, Chris Mckee and Martin Houde and for detailed suggestions that significantly improved the manuscript. A.L. acknowledges the support the NSF AST 1816234, NASA TCAN 144AAG1967 and NASA ATP AAH7546. Flatiron Institute is supported by the Simons Foundation. This research used resources provided by the Los Alamos National Laboratory Institutional Computing Program, which is supported by the U.S. Department of Energy National Nuclear Security Administration under Contract No. 89233218CNA000001.

This research also used resources of the National Energy Research Scientific Computing Center (NERSC), a U.S. Department of Energy Office of Science User Facility located at Lawrence Berkeley National Laboratory, operated under Contract No. DE-AC02-05CH11231 using NERSC award FES-ERCAP-m4239 (PI: KHY, LANL). D.P. thanks Theoretical Group at Korea Astronomy and Space Science Institute (KASI) for hospitality. Flatiron Institute is supported by Simons Foundation. Research presented in this article was supported by the Laboratory Directed Research and Development program of Los Alamos National Laboratory under project number(s) 20220700PRD1. This research was supported in part by grant NSF PHY-2309135 to the Kavli Institute for Theoretical Physics (KITP).

Data Availability The data underlying this article will be shared on reasonable request to the corresponding author. The code can be found in https://github.com/kyuen2/MHD_modes

APPENDIX

A. GRADIENT VARIANCE AND ITS DEPENDENCE ON M_A AND γ

A.1. Gradient methods to study magnetic field

Let us briefly summarize the mathematical foundations of the gradient methods in application to study of the direction of the magnetic field. The formalism was developed in Fourier space in Lu et al. (2020). Here we complement the exposition by real space treatment, as well as add more details.

Let us denote by $f(\mathbf{X})$ a sky map of observable emission from a turbulent medium. For example, this can be the intensity of the emission in PPV (position-position \mathbf{X} -velocity v) space $I(\mathbf{X}, v)$, or the related integrated quantities, such as the total intensity $I_c(\mathbf{X}) \propto \int dv I(\mathbf{X}, v)$ or velocity centroids which for optically thin lines are $VC(\mathbf{X}) \propto \int v dv I(\mathbf{X}, v)$.

The simplest local statistical measure for the gradient of a random field $f(\mathbf{X})$ is the gradient covariance tensor

$$\sigma_{ij} \equiv \langle \nabla_i f(\mathbf{X}) \nabla_j f(\mathbf{X}) \rangle = \nabla_i \nabla_j D(\mathbf{R})|_{\mathbf{R} \rightarrow 0} \quad (\text{A1})$$

which is the zero separation limit of the second derivatives of the field structure function $D(\mathbf{R}) \equiv \frac{1}{2} \langle (f(\mathbf{X} + \mathbf{R}) - f(\mathbf{X}))^2 \rangle$.

For a statistically isotropic field, the covariance of the gradients is isotropic, $\sigma_{\nabla_i \nabla_j} = \frac{1}{2} \delta_{ij} \Delta D(\mathbf{R})|_{\mathbf{R} \rightarrow 0}$. In the presence of the magnetic field, the structure function of the signal becomes orientation dependent, depending on the angle between \mathbf{R} and the projected direction of the magnetic field. This anisotropy is retained in the limit $\mathbf{R} \rightarrow 0$ and results in non-vanishing traceless part of the gradient covariance tensor

$$\sigma_{ij} - \frac{1}{2} \delta_{ij} \sum_{l=1,2} \sigma_{ll} = \frac{1}{2} \begin{pmatrix} (\nabla_x^2 - \nabla_y^2) D(\mathbf{R}) & 2\nabla_x \nabla_y D(\mathbf{R}) \\ 2\nabla_x \nabla_y D(\mathbf{R}) & (\nabla_y^2 - \nabla_x^2) D(\mathbf{R}) \end{pmatrix}_{\mathbf{R} \rightarrow 0} \neq 0 \quad (\text{A2})$$

As a rank two symmetric tensor, gradient covariance has two rotational invariants, the trace and the determinant, or, correspondingly, the determinant of the traceless part. Thus, in our case we can introduce invariant I_0 and I_2

$$\sigma_{xx} + \sigma_{yy} = I_0 \quad (\text{A3})$$

$$(\sigma_{xx} - \sigma_{yy})^2 + 4\sigma_{xy}^2 = I_2^2 \quad (\text{A4})$$

Their dimensionless ratio is important as a measure of anisotropy level

$$J_2 \equiv \frac{(\sigma_{xx} - \sigma_{yy})^2 + 4\sigma_{xy}^2}{(\sigma_{xx} + \sigma_{yy})^2} = \left(\frac{I_2}{I_0} \right)^2 \quad (\text{A5})$$

We now study anisotropy by decomposing the structure function in angular harmonics, which can be done either in Fourier space or real space.

A.1.1. *Fourier space evaluation of gradient covariance tensor*

In Fourier space, where

$$D(\mathbf{R}) = \int d\mathbf{K} P(\mathbf{K}) [1 - e^{i\mathbf{K}\cdot\mathbf{R}}] , \quad (\text{A6})$$

the angular decomposition is over the dependence of the power spectrum $P(\mathbf{K})$ on the angle of the 2D wave vector \mathbf{K} . Denoting the coordinate angle of \mathbf{K} by θ_K and that of the projected magnetic field as θ_H , we have for the spectrum

$$P(\mathbf{K}) = \sum_n P_n(K) e^{in(\theta_H - \theta_K)} \quad (\text{A7})$$

and for the derivatives of the structure function

$$\nabla_i \nabla_j D(\mathbf{R}) = \sum_n \int K^3 P_n(K) \int d\theta_K e^{in(\theta_H - \theta_K)} e^{iKR \cos(\theta_R - \theta_K)} \hat{K}_i \hat{K}_j , \quad (\text{A8})$$

where hat designates unit vectors, namely $\hat{K}_x = \cos \theta_K$ and $\hat{K}_y = \sin \theta_K$. Performing integration over θ_K , we obtain the traceless anisotropic part that involves Bessel functions $J_n(KR)$

$$\begin{aligned} (\nabla_x^2 - \nabla_y^2) D(\mathbf{R}) &= \pi \sum_n i^n e^{in(\theta_H - \theta_R)} \int dK K^3 J_n(kR) (P_{n-2}(K) e^{-i2\theta_H} + P_{n+2}(K) e^{i2\theta_H}) \\ \nabla_x \nabla_y D(\mathbf{R}) &= \frac{\pi}{2i} \sum_n i^n e^{in(\theta_H - \theta_R)} \int dK K^3 J_n(kR) (-P_{n-2}(K) e^{-i2\theta_H} + P_{n+2}(K) e^{i2\theta_H}) \end{aligned} \quad (\text{A9})$$

In the limit $R \rightarrow 0$, only $n = 0$ term for which $J_0(0) = 1$ survives, θ_R dependence drops out, and we have

$$\begin{aligned} (\nabla_x^2 - \nabla_y^2) D(\mathbf{R}) &= \left[2\pi \int dK K^3 P_2(K) \right] \cos 2\theta_H \\ 2\nabla_x \nabla_y D(\mathbf{R}) &= \left[2\pi \int dK K^3 P_2(K) \right] \sin 2\theta_H \end{aligned} \quad (\text{A10})$$

We can now identify I_2 invariants with the integral over spectrum multipoles

$$I_2 = 2\pi \int dK K^3 P_2(K) \quad (\text{A11})$$

Notice that anisotropy of the gradient variance is determined by the quadrupole of the power spectrum as expected.

A.1.2. *Real space approach to evaluating gradient covariance tensor*

Now we demonstrate how gradient covariance tensor can be evaluated in the real space to link it explicitly to the multipole decomposition structure-function function that can be performed locally.

We need to compute $R \rightarrow 0$ limit of the structure function derivatives that we represent in polar coordinates as

$$\begin{aligned} (\nabla_x^2 - \nabla_y^2) D(R, \theta_R) &= \cos 2\theta_R \left(R \frac{\partial}{\partial R} \frac{1}{R} \frac{\partial}{\partial R} - \frac{1}{R^2} \frac{\partial^2}{\partial \theta_R^2} \right) D(R, \theta_R) - \sin 2\theta_R \frac{\partial}{\partial R} \left(\frac{2}{R} \frac{\partial}{\partial \theta_R} \right) D(R, \theta_R) \\ 2\nabla_x \nabla_y D(R, \theta_R) &= \sin 2\theta_R \left(R \frac{\partial}{\partial R} \frac{1}{R} \frac{\partial}{\partial R} - \frac{1}{R^2} \frac{\partial^2}{\partial \theta_R^2} \right) D(R, \theta_R) + \cos 2\theta_R \frac{\partial}{\partial R} \left(\frac{2}{R} \frac{\partial}{\partial \theta_R} \right) D(R, \theta_R) \\ (\nabla_x^2 + \nabla_y^2) D(R, \theta_R) &= \left(\frac{1}{R} \frac{\partial}{\partial R} R \frac{\partial}{\partial R} + \frac{1}{R^2} \frac{\partial^2}{\partial \theta_R^2} \right) D(R, \theta_R) \end{aligned} \quad (\text{A12})$$

where we added the trace for completeness, but also for the future use.

We present $D(R, \theta_R)$ as an expansion in the eigenfunctions of the Laplace operator, $\Delta f_{K_n}(R, \theta) = -K^2 f_{K_n}(R, \theta)$, subject to the boundary condition $D(0, \theta_R) = 0$. Choosing angular directions in respect to symmetry direction θ_H we have multipole expansion

$$D(R, \theta_R) = \sum_n D_n(R) e^{in(\theta_R - \theta_H)} \quad (\text{A13})$$

with radial functions expanded in the Bessel function series

$$D_n(R) = D_{-n}(R) = 2\pi \int K dK P_n(K) (\delta_{n0} - i^n J_{|n|}(KR)) \quad (\text{A14})$$

where δ_{n0} term enforces the boundary condition. Note, that though it looks very much as a Fourier expansion, here we can have a local expansion of the structure function in the vicinity of some fixed point in space (from which R separation is measured) instead of global expansion into plane waves. Thus, we can use this expansion in a statistically inhomogeneous situation, one patch at a time, especially that we are interested in $R \rightarrow 0$ limit.

We need to determine the action of three differential operators on the multipole coefficients $D_n(R)$ which we expect to give

$$\begin{aligned} \lim_{R \rightarrow 0} \left(R \frac{\partial}{\partial R} \frac{1}{R} \frac{\partial}{\partial R} + \frac{n^2}{R^2} \right) D_n(R) &= \frac{1}{2} (\delta_{n,2} + \delta_{n,-2}) I_2 \\ \lim_{R \rightarrow 0} 2i n \frac{\partial}{\partial R} \frac{1}{R} D_n(R) &= \frac{i}{2} (\delta_{n,2} - \delta_{n,-2}) I_2 \\ \lim_{R \rightarrow 0} \left(\frac{1}{R} \frac{\partial}{\partial R} R \frac{\partial}{\partial R} - \frac{n^2}{R^2} \right) D_n(R) &= \delta_{n0} I_0 \end{aligned} \quad (\text{A15})$$

To prove these relations and determine I_0 and I_2 , we differentiate the Bessel functions as $J_n(x)' = -J_{n+1}(x) + nJ_n(x)/x$ and, if needed, use the recurrence relation in the direction of eliminating the divergent terms as we take the limit $x \rightarrow 0$. Our first combination is

$$\begin{aligned} \frac{\partial}{\partial R} \frac{J_n(KR)}{R} &= \frac{K^2}{x} (J_n(x)' - J_n(x)/x) \\ &= K^2 \left(-\frac{J_{n+1}(x)}{x} + \frac{n-1}{x^2} J_n(x) \right) \\ &\rightarrow \frac{1}{8} K^2 \delta_{n,2} - K^2 \delta_{n0} \left(\frac{1}{2} + \frac{J_0}{x^2} \right) \end{aligned} \quad (\text{A16})$$

where divergent at $R \rightarrow 0$ $n = 0$ term does not contribute to the final result since we multiply this derivative by n .

The other combination is

$$\begin{aligned} \left(R \frac{\partial}{\partial R} \frac{1}{R} \frac{\partial}{\partial R} + \frac{n^2}{R^2} \right) J_n(KR) &= K^2 \left(x \frac{\partial}{\partial x} \frac{1}{x} \left(-J_{n+1}(x) + \frac{n}{x} J_n(x) \right) + \frac{n^2}{x^2} J_n(x) \right) \\ &= K^2 \left(J_{n+2}(x) - \frac{2n}{x} J_{n+1}(x) + \frac{2n(n-1)}{x^2} J_n(x) \right) \\ &\rightarrow \frac{1}{2} K^2 \delta_{n,2} \end{aligned} \quad (\text{A17})$$

For the last combination (which is the Laplacian) the answer is already known

$$\left(\frac{1}{R} \frac{\partial}{\partial R} R \frac{\partial}{\partial R} - \frac{n^2}{R^2} \right) J_n(KR) = -K^2 J_n(x) \rightarrow -K^2 \delta_{n,0} \quad (\text{A18})$$

Using Eqs. (A16-A18) leads to the result Eq. (A15) with $I_n = 2\pi \int dK K^3 P_n(K)$. Taking $R \rightarrow 0$ limit in Eq. (A14) shows that in the real space formulation the invariants are given by

$$I_0 = 4 \lim_{R \rightarrow 0} D_0(R)/R^2 \quad (\text{A19})$$

$$I_2 = 8 \lim_{R \rightarrow 0} D_2(R)/R^2. \quad (\text{A20})$$

Finally, substituting Eqs. (A15) into Eq. (A14) and then Eqs. (A12) we confirm that the dependence on the position vector angle cancels in the covariance matrix as it takes the expected form

$$\begin{aligned} \sigma_{xx} - \sigma_{yy} &= \frac{I_2}{2} \left(\cos 2\theta_R \left(e^{2i(\theta_R - \theta_H)} + e^{-2i(\theta_R - \theta_H)} \right) - i \sin 2\theta_R \left(e^{2i(\theta_R - \theta_H)} - e^{-2i(\theta_R - \theta_H)} \right) \right) = I_2 \cos 2\theta_H \\ 2\sigma_{xy} &= \frac{I_2}{2} \left(\sin 2\theta_R \left(e^{2i(\theta_R - \theta_H)} + e^{-2i(\theta_R - \theta_H)} \right) + i \cos 2\theta_R \left(e^{2i(\theta_R - \theta_H)} - e^{-2i(\theta_R - \theta_H)} \right) \right) = I_2 \sin 2\theta_H \\ \sigma_{xx} + \sigma_{yy} &= I_0 \end{aligned} \quad (\text{A21})$$

A.1.3. Eigendirections of the gradient covariance tensor

The eigendirection of the covariance tensor that corresponds to the largest eigenvalue (“the direction of the gradient”) makes an angle θ with the coordinate x-axis

$$\tan \theta = \frac{2\nabla_x \nabla_y D}{\sqrt{(\nabla_x^2 D - \nabla_y^2 D)^2 + 4(\nabla_x \nabla_y D)^2 + (\nabla_x^2 + \nabla_y^2) D}}. \quad (\text{A22})$$

Substituting expressions for derivatives into this formula we find that the eigendirection of the gradient variance has the form

$$\tan \theta = \frac{A \sin 2\theta_H}{|A| + A \cos 2\theta_H} = \begin{cases} \tan \theta_H & A > 0 \\ -\cot \theta_H & A < 0 \end{cases} \quad (\text{A23})$$

and is either parallel or perpendicular to the direction of the magnetic field, depending on the sign of $A \propto \int dK K^3 P_2(K)$, i.e the sign of the spectral quadrupole P_2 .

Since the direction of the magnetic field that we aim to track is unsigned, it is appropriate to describe it as an eigendirection of the rank-2 tensor, rather than a vector. This naturally leads to the mathematical formalism of Stokes parameters. We can introduce local pseudo-Stokes parameters built from the field gradients

$$\tilde{Q} \propto (\nabla_x f)^2 - (\nabla_y f)^2 \quad (\text{A24})$$

$$\tilde{U} \propto 2\nabla_x f \nabla_y f \quad (\text{A25})$$

which averages are directly linked to statistics of the gradients

$$\langle \tilde{Q} \rangle \propto \sigma_{xx}^2 - \sigma_{yy}^2 = I_2 \cos 2\theta_H \quad (\text{A26})$$

$$\langle \tilde{U} \rangle \propto 2\sigma_{xy}^2 = I_2 \sin 2\theta_H \quad (\text{A27})$$

and give the estimate of the direction of the magnetic field

$$\frac{\langle \tilde{U} \rangle}{\langle \tilde{Q} \rangle} = \tan 2\theta_H \quad (\text{A28})$$

The pseudo Stokes parameters naturally connect the gradient techniques with polarization studies.

A.2. Distribution of gradient angles, J_2 as a measure of anisotropy

As a model distribution of the gradient angle evaluate in the pixel p , $\theta_p = \text{atan}[\nabla_y I / \nabla_x I]$, we take the distribution that follows from assuming the gradients to be Gaussian with the covariance matrix $\tilde{\sigma}_{ij}$ of Eq.16. The expression for this distribution can be easily obtained as:

$$P(\theta_p) = \frac{1}{\pi \sqrt{|\sigma_{ij}|}} \left[\begin{pmatrix} \cos \theta_p \\ \sin \theta_p \end{pmatrix} \sigma_{ij}^{-1} \begin{pmatrix} \cos \theta_p \\ \sin \theta_p \end{pmatrix} \right]^{-1} \quad (\text{A29})$$

$$= \frac{1}{\pi} \times \frac{\sqrt{1 - J_2}}{1 - \sqrt{J_2} \cos 2(\theta_H - \theta_p)} \quad (\text{A30})$$

This distribution function has two parameters: J_2 and θ_H . The first is the rotation invariant ratio of the determinant of the traceless part of the covariance matrix and the (half of) trace of the covariance

$$J_2 \equiv \frac{(\sigma_{xx} - \sigma_{yy})^2 + 4\sigma_{xy}^2}{(\sigma_{xx} + \sigma_{yy})^2} = 4 \left(\lim_{R \rightarrow 0} \frac{D_2(R)}{D_0(R)} \right)^2 \quad (\text{A31})$$

and the second is the angle

$$\tan 2\theta_H \equiv \frac{2\sigma_{xy}}{\sigma_{xx} - \sigma_{yy}} \quad (\text{A32})$$

The distribution in Eq.(A29) is periodic with a period π and is normalized to unity on any angular interval of the length of the period, $\int_{\theta_p^*}^{\theta_p^* + \pi} P(\theta_p) d\theta_p = 1$. Statistically isotropic case corresponds to $\sigma_{xx} = \sigma_{yy}$ and $\sigma_{xy} = 0$, i.e $J_2 = 0$ when Eq.(A29) evaluates to uniform distribution. Any anisotropy leads to non-zero $J_2 > 0$, which on the other hand is bounded by definition not to exceed unity, $J_2 \leq 1$. Note that fitting angular distribution does not determine the trace of gradient covariance I_0 .

B. ADDITIONAL TOOLS COMPLEMENTARY TO THE CURRENT PAPER

Most of the current paper describes how to estimate magnetic field within the framework of the Velocity Gradient Technique (VGT). However, the techniques that are developed in the current paper does not require the prediction from the gradient technique to work. In the following, we discuss the complementary techniques that can help us to construct the 3D distribution of magnetic field.

B.1. Obtaining M_s , M_A and the inclination angle γ

Alfvénic Mach number M_A : For instance, the ability of various techniques to estimate the values of M_A and M_s from observational data were studied in literature prior to the time of GT appeared. For instance, the ability of Tsallis statistics to obtain M_A was demonstrated in [Esquivel & Lazarian \(2010\)](#) and [Tofflemire et al. \(2011\)](#). In addition, [Esquivel & Lazarian \(2005\)](#) obtained empirical relations between the anisotropy of the structure function and M_A . In fact, the first demonstration of the effect of magnetic field strength on the anisotropy of correlations in the channel maps was presented in [Lazarian et al. \(2002\)](#). The analytical relations between M_A the ratio of the quadrupole to monopole moments of the structure functions of intensity was obtained in LP12 for synchrotron emission and in KLP17, [Kandel et al. \(2017b\)](#) and [Kandel et al. \(2018\)](#) for the spectroscopic data. The ability of obtaining the mean M_A was demonstrated with polarization data in [Lazarian et al. \(2018\)](#), while the statistics of M_A was carefully studied in [Yuen & Lazarian \(2020b\)](#).

Sonic Mach number M_s : It its turn, M_s was obtained via the analysis of kurtosis and skewness of the emission and polarization observational data (see [Burkhart et al. 2009](#); [Burkhart & Lazarian 2012](#); [Burkhart et al. 2013, 2014](#)). Combining thus found M_s with the M_A obtained with the approaches above ,one can successfully obtain the strength of the POS component of the magnetic field. The results of M_s measurements are very robust, and they are marginally affected either by shear or by large-scale magnetic field curvature. Similarly, the calculation of M_A is not much influenced by the galactic shear or any other large-scale shear induced by non-turbulent motions.

Inclination Angle γ : To obtain the full magnetic field strength, an independent way of obtaining γ is necessary. Different measures depend differently on the aforementioned turbulence parameters and γ . This provides another avenue for obtaining the 3D vector of the magnetic field. Several approaches for obtaining γ are suggested and explored in [Yuen et al. \(2023\)](#); [Malik et al. \(2023, 2024\)](#) and [Hu et al. \(2024\)](#); [Hu & Lazarian \(2024\)](#). If combined with the value of the magnetic field obtained with the DMA approach, the output provides the full 3D magnetic field vector.

B.2. Removing density contributions when computing gradients

As we discussed earlier, MHD turbulence theory is defined in terms of velocity and magnetic field fluctuations (see [Beresnyak & Lazarian 2019](#)). The density can act either as a passive scalar or show its own non-universal scaling. The former is mostly the case of subsonic turbulence and this, as pointed out in §3.5 results in the density gradient technique. However, in general, one can get more reliable predictions if the density contributions are removed.

It is worth emphasizing that the most of the previous predictions on Alfvénic Mach number in both the LP-series or the KLP series assume a constant density and negligible thermal broadening effects. While the authors have discussed qualitatively how these effects change the analytical predictions, it is unavoidable to deal with both the density and thermal effects in regimes such as multiphase HI media. To remove the effects of density and thermal broadening from observed channels, [Yuen et al. \(2021\)](#) proposes the **Velocity Decomposition Algorithm (VDA)**, an algorithm that is built upon the foundation of LP00, that applies to every channel map. The *velocity caustics* map p_v , which is the channel map without any density fluctuations, is given by:

$$p_v = p - (\langle pI \rangle - \langle p \rangle \langle I \rangle) \frac{I - \langle I \rangle}{\sigma_I^2} \quad (\text{B33})$$

where p is the channel map, I is the column density map and $\langle \dots \rangle$ is the averaging operator. [Yuen et al. \(2021\)](#) shows that the VDA method is extremely accurate reflecting the statistics of velocity fluctuations in sub-sonic media while being fairly accurate in supersonic media. For our current paper's purpose, we need the velocity centroid map with no density effects. The appendix of [Yuen et al. \(2021\)](#) gives a formula for the constant density velocity centroid:

$$V_n(\mathbf{X}) = \int dv v p_v(\mathbf{X}, v) \quad (\text{B34})$$

which is exactly the quantity that is investigated in both [KLP16](#) and [KLP17](#). Note, that in this paper we use capital symbols to denote the 2D vectors, i.e. \mathbf{X} is the 2D Plane of Sky (POS) vector. In below we are going to investigate the gradients of centroid or channels *assuming density being constant*. The exact formula in obtaining these observables are given by either Eq.B33 (channels) or Eq.B34 (centroids).

B.3. Obtaining 3D magnetic field structures from divergence free condition

It was discussed in Lazarian & Yuen (2018b) that the 3D distribution of POS magnetic field can be obtained applying velocity gradients to channel maps or reduced centroids and using the galactic rotation curve. This approach was applied in González-Casanova & Lazarian (2019) to map the POS magnetic field using gradients of the velocity centroids. The corresponding map of 3D distribution of the POS magnetic field was then successfully tested by comparing the starlight polarization predicted for a number of stars with the known distances with the actual measured polarization.

The ability of obtaining 3D POS B-field maps provide another way of obtaining the actual distribution of 3D magnetic field vectors. Indeed, the magnetic field is a solenoidal vector three components of which are constrained through the divergence free condition: $\nabla \cdot \mathbf{B} = 0$, meaning that that only 2 components in Fourier space are independent. Therefore if we are given 2 components, we can restore the 3d one. The corresponding procedure was suggested in Chepurnov (2021) for restoring the z-component of magnetic field when two POS component are obtained using the Lazarian & Yuen (2018b) synchrotron gradient tomography that can restore the 3D POS magnetic field.

We would like to stress that the same procedure is also applicable to studying magnetic fields using both the POS magnetic fields obtained using the channel maps or reduced centroids in the presence of galactic rotation curve. The caveat for the application of the technique is that the magnetic field is solenoidal in actual 3D space and can lose this property in other coordinates. For instance, the distortions of the 2D slice for which the POS magnetic field is determined can result in errors in determining the LOS component of magnetic field. This means that the POS for the procedure should be sufficiently coarse grained to avoid problems of the mapping.

C. NUMERICAL SIMULATIONS EMPLOYED FOR TESTING

In Table 1 we describe the set of numerical simulations that we employ to test our analytical results.

Model	M_S	M_A	$\beta = 2M_A^2/M_S^2$	Resolution	Model	M_S	M_A	$\beta = 2M_A^2/M_S^2$	Resolution
b11	0.41	0.04	0.02	480 ³	huge-0	6.17	0.22	0.0025	792 ³
b12	0.92	0.09	0.02	480 ³	huge-1	5.65	0.42	0.011	792 ³
b13	1.95	0.18	0.02	480 ³	huge-2	5.81	0.61	0.022	792 ³
b14	3.88	0.35	0.02	480 ³	huge-3	5.66	0.82	0.042	792 ³
b15	7.14	0.66	0.02	480 ³	huge-4	5.62	1.01	0.065	792 ³
b21	0.47	0.15	0.22	480 ³	huge-5	5.63	1.19	0.089	792 ³
b22	0.98	0.32	0.22	480 ³	huge-6	5.70	1.38	0.12	792 ³
b23	1.92	0.59	0.22	480 ³	huge-7	5.56	1.55	0.16	792 ³
b31	0.48	0.48	2.0	480 ³	huge-8	5.50	1.67	0.18	792 ³
b32	0.93	0.94	2.0	480 ³	huge-9	5.39	1.71	0.20	792 ³
b41	0.16	0.49	18	480 ³	h0-1200	6.36	0.22	0.0025	1200 ³
b42	0.34	1.11	18	480 ³	h9-1200	10.79	2.29	0.098	1200 ³
b51	0.05	0.52	200	480 ³	e5r2	0.13	5.99	4363	1200 ³
b52	0.10	1.08	200	480 ³	e5r3	0.61	0.63	2.09	1200 ³
Ms0.2Ma0.2	0.2	0.2	2	480 ³	e6r3	5.45	0.50	0.017	1200 ³
Ms0.4Ma0.2	0.57	0.28	0.48	480 ³	e7r3	0.53	3.24	73.64	1200 ³
Ms4.0Ma0.2	3.81	0.18	0.00446	480 ³	incompressible	0	0.61	∞	512 ³
Ms20.0Ma0.2	20.59	0.18	0.00015	480 ³					

Table 1. Description of MHD simulation cubes which some of them have been used in the series of papers about VGT (Yuen & Lazarian 2017a,b; Lazarian & Yuen 2018b,a). M_s and M_A are the R.M.S values at each the snapshots are taken. The incompressible simulation is performed by Ho (2022).

REFERENCES

- Andersson, B. G., Lazarian, A., & Vaillancourt, J. E. 2015a, ARA&A, 53, 501, doi: 10.1146/annurev-astro-082214-122414
- , 2015b, ARA&A, 53, 501, doi: 10.1146/annurev-astro-082214-122414

- Armstrong, J. W., Rickett, B. J., & Spangler, S. R. 1995, *ApJ*, 443, 209, doi: [10.1086/175515](https://doi.org/10.1086/175515)
- Beattie, J. R., Krumholz, M. R., Federrath, C., Sampson, M. L., & Crocker, R. M. 2022, *Frontiers in Astronomy and Space Sciences*, 9, 900900, doi: [10.3389/fspas.2022.900900](https://doi.org/10.3389/fspas.2022.900900)
- Beck, R. 2015, in *Astrophysics and Space Science Library*, Vol. 407, *Magnetic Fields in Diffuse Media*, ed. A. Lazarian, E. M. de Gouveia Dal Pino, & C. Melioli, 507, doi: [10.1007/978-3-662-44625-6_18](https://doi.org/10.1007/978-3-662-44625-6_18)
- Beresnyak, A., & Lazarian, A. 2019, *Turbulence in Magnetohydrodynamics* (Berlin, Boston: De Gruyter), doi: [doi:10.1515/9783110263282](https://doi.org/10.1515/9783110263282)
- Beresnyak, A., & Lazarian, A. 2019, *Turbulence in Magnetohydrodynamics*
- Beresnyak, A., Lazarian, A., & Cho, J. 2005, *ApJL*, 624, L93, doi: [10.1086/430702](https://doi.org/10.1086/430702)
- Burkhart, B., Falceta-Gonçalves, D., Kowal, G., & Lazarian, A. 2009, *ApJ*, 693, 250, doi: [10.1088/0004-637X/693/1/250](https://doi.org/10.1088/0004-637X/693/1/250)
- Burkhart, B., & Lazarian, A. 2012, *ApJL*, 755, L19, doi: [10.1088/2041-8205/755/1/L19](https://doi.org/10.1088/2041-8205/755/1/L19)
- Burkhart, B., Lazarian, A., & Gaensler, B. M. 2012, *ApJ*, 749, 145, doi: [10.1088/0004-637X/749/2/145](https://doi.org/10.1088/0004-637X/749/2/145)
- Burkhart, B., Lazarian, A., Leão, I. C., de Medeiros, J. R., & Esquivel, A. 2014, *ApJ*, 790, 130, doi: [10.1088/0004-637X/790/2/130](https://doi.org/10.1088/0004-637X/790/2/130)
- Burkhart, B., Lazarian, A., Ossenkopf, V., & Stutzki, J. 2013, *ApJ*, 771, 123, doi: [10.1088/0004-637X/771/2/123](https://doi.org/10.1088/0004-637X/771/2/123)
- Carmo, L., González-Casanova, D. F., Falceta-Gonçalves, D., et al. 2020, *ApJ*, 905, 130, doi: [10.3847/1538-4357/abc331](https://doi.org/10.3847/1538-4357/abc331)
- Chandrasekhar, S., & Fermi, E. 1953, *ApJ*, 118, 113, doi: [10.1086/145731](https://doi.org/10.1086/145731)
- Chepurnov, A. 2021, arXiv e-prints, arXiv:2107.05070, doi: [10.48550/arXiv.2107.05070](https://doi.org/10.48550/arXiv.2107.05070)
- Chepurnov, A., Burkhart, B., Lazarian, A., & Stanimirovic, S. 2015, *ApJ*, 810, 33, doi: [10.1088/0004-637X/810/1/33](https://doi.org/10.1088/0004-637X/810/1/33)
- Chepurnov, A., Gordon, J., Lazarian, A., & Stanimirovic, S. 2008, *ApJ*, 688, 1021, doi: [10.1086/591655](https://doi.org/10.1086/591655)
- Chepurnov, A., & Lazarian, A. 2009, *ApJ*, 693, 1074, doi: [10.1088/0004-637X/693/2/1074](https://doi.org/10.1088/0004-637X/693/2/1074)
- . 2010, *ApJ*, 710, 853, doi: [10.1088/0004-637X/710/1/853](https://doi.org/10.1088/0004-637X/710/1/853)
- Cho, J., & Lazarian, A. 2002, *PhRvL*, 88, 245001, doi: [10.1103/PhysRevLett.88.245001](https://doi.org/10.1103/PhysRevLett.88.245001)
- . 2003, *MNRAS*, 345, 325, doi: [10.1046/j.1365-8711.2003.06941.x](https://doi.org/10.1046/j.1365-8711.2003.06941.x)
- Cho, J., Lazarian, A., & Vishniac, E. T. 2002, *ApJ*, 564, 291, doi: [10.1086/324186](https://doi.org/10.1086/324186)
- Cho, J., & Vishniac, E. T. 2000, *ApJ*, 539, 273, doi: [10.1086/309213](https://doi.org/10.1086/309213)
- Cho, J., & Yoo, H. 2016, *ApJ*, 821, 21, doi: [10.3847/0004-637X/821/1/21](https://doi.org/10.3847/0004-637X/821/1/21)
- Clarke, D. A. 2010, *ApJS*, 187, 119, doi: [10.1088/0067-0049/187/1/119](https://doi.org/10.1088/0067-0049/187/1/119)
- Crutcher, R. M. 2004, *Ap&SS*, 292, 225, doi: [10.1023/B:ASTR.0000045021.42255.95](https://doi.org/10.1023/B:ASTR.0000045021.42255.95)
- Davis, L. 1951, *Physical Review*, 81, 890, doi: [10.1103/PhysRev.81.890.2](https://doi.org/10.1103/PhysRev.81.890.2)
- Draine, B. T. 2009, in *Astronomical Society of the Pacific Conference Series*, Vol. 414, *Cosmic Dust - Near and Far*, ed. T. Henning, E. Grün, & J. Steinacker, 453, <https://arxiv.org/abs/0903.1658>
- Elmegreen, B. G., & Scalo, J. 2004, *ARA&A*, 42, 211, doi: [10.1146/annurev.astro.41.011802.094859](https://doi.org/10.1146/annurev.astro.41.011802.094859)
- Esquivel, A., & Lazarian, A. 2005, *ApJ*, 631, 320, doi: [10.1086/432458](https://doi.org/10.1086/432458)
- . 2010, *ApJ*, 710, 125, doi: [10.1088/0004-637X/710/1/125](https://doi.org/10.1088/0004-637X/710/1/125)
- Falceta-Gonçalves, D., Lazarian, A., & Kowal, G. 2008, *ApJ*, 679, 537, doi: [10.1086/587479](https://doi.org/10.1086/587479)
- Gaensler, B. M., Haverkorn, M., Burkhart, B., et al. 2011, *Nature*, 478, 214, doi: [10.1038/nature10446](https://doi.org/10.1038/nature10446)
- Galli, D., Lizano, S., Shu, F. H., & Allen, A. 2006, *ApJ*, 647, 374, doi: [10.1086/505257](https://doi.org/10.1086/505257)
- Galtier, S., Nazarenko, S. V., Newell, A. C., & Pouquet, A. 2000, *Journal of Plasma Physics*, 63, 447, doi: [10.1017/S0022377899008284](https://doi.org/10.1017/S0022377899008284)
- Girart, J. M., Rao, R., & Marrone, D. P. 2006, *Science*, 313, 812, doi: [10.1126/science.1129093](https://doi.org/10.1126/science.1129093)
- Goldreich, P., & Kylafis, N. D. 1981, *ApJL*, 243, L75, doi: [10.1086/183446](https://doi.org/10.1086/183446)
- Goldreich, P., & Sridhar, S. 1995, *ApJ*, 438, 763, doi: [10.1086/175121](https://doi.org/10.1086/175121)
- González-Casanova, D. F., & Lazarian, A. 2017, *ApJ*, 835, 41, doi: [10.3847/1538-4357/835/1/41](https://doi.org/10.3847/1538-4357/835/1/41)
- . 2019, *ApJ*, 874, 25, doi: [10.3847/1538-4357/ab0552](https://doi.org/10.3847/1538-4357/ab0552)
- Habegger, R., Ho, K. W., Yuen, K. H., & Zweibel, E. G. 2024, arXiv e-prints, arXiv:2403.07976, doi: [10.48550/arXiv.2403.07976](https://doi.org/10.48550/arXiv.2403.07976)
- Hayes, J. C., Norman, M. L., Fiedler, R. A., et al. 2006, *ApJS*, 165, 188, doi: [10.1086/504594](https://doi.org/10.1086/504594)
- Heitsch, F., Zweibel, E. G., Mac Low, M.-M., Li, P., & Norman, M. L. 2001, *ApJ*, 561, 800, doi: [10.1086/323489](https://doi.org/10.1086/323489)
- Heyer, M., Gong, H., Ostriker, E., & Brunt, C. 2008, *ApJ*, 680, 420, doi: [10.1086/587510](https://doi.org/10.1086/587510)
- Heyer, M. H., & Brunt, C. M. 2004, *ApJL*, 615, L45, doi: [10.1086/425978](https://doi.org/10.1086/425978)
- Ho, K. W. 2022, *MHDFlows.jl*, v.0.2.1b, Zenodo, doi: [10.5281/zenodo.8242702](https://doi.org/10.5281/zenodo.8242702)
- Ho, K. W., & Lazarian, A. 2021, *ApJ*, 911, 53, doi: [10.3847/1538-4357/abe713](https://doi.org/10.3847/1538-4357/abe713)
- . 2023, *MNRAS*, 520, 3857, doi: [10.1093/mnras/stad186](https://doi.org/10.1093/mnras/stad186)

- Ho, K. W., Yuen, K. H., & Lazarian, A. 2023, *MNRAS*, 521, 230, doi: [10.1093/mnras/stad481](https://doi.org/10.1093/mnras/stad481)
- Ho, K. W., Yuen, K. H., Leung, P. K., & Lazarian, A. 2019, *ApJ*, 887, 258, doi: [10.3847/1538-4357/ab578c](https://doi.org/10.3847/1538-4357/ab578c)
- Houde, M. 2004, *ApJL*, 616, L111, doi: [10.1086/426684](https://doi.org/10.1086/426684)
- Hu, Y., & Lazarian, A. 2023a, *MNRAS*, 524, 2379, doi: [10.1093/mnras/stad1996](https://doi.org/10.1093/mnras/stad1996)
- . 2023b, *MNRAS*, 524, 4431, doi: [10.1093/mnras/stad2158](https://doi.org/10.1093/mnras/stad2158)
- . 2024, arXiv e-prints, arXiv:2404.07806, doi: [10.48550/arXiv.2404.07806](https://doi.org/10.48550/arXiv.2404.07806)
- Hu, Y., Lazarian, A., & Stanimirović, S. 2021, *ApJ*, 912, 2, doi: [10.3847/1538-4357/abedb7](https://doi.org/10.3847/1538-4357/abedb7)
- Hu, Y., Lazarian, A., Wu, Y., & Fu, C. 2024, *MNRAS*, 527, 11240, doi: [10.1093/mnras/stad3766](https://doi.org/10.1093/mnras/stad3766)
- Hu, Y., Lazarian, A., & Yuen, K. H. 2020a, *ApJ*, 897, 123, doi: [10.3847/1538-4357/ab9948](https://doi.org/10.3847/1538-4357/ab9948)
- Hu, Y., Yuen, K. H., & Lazarian, A. 2019a, *ApJ*, 886, 17, doi: [10.3847/1538-4357/ab4b5e](https://doi.org/10.3847/1538-4357/ab4b5e)
- . 2019b, *ApJ*, 886, 17, doi: [10.3847/1538-4357/ab4b5e](https://doi.org/10.3847/1538-4357/ab4b5e)
- . 2020b, *ApJ*, 888, 96, doi: [10.3847/1538-4357/ab60a5](https://doi.org/10.3847/1538-4357/ab60a5)
- Hu, Y., Yuen, K. H., Lazarian, A., et al. 2019c, *ApJ*, 884, 137, doi: [10.3847/1538-4357/ab41f2](https://doi.org/10.3847/1538-4357/ab41f2)
- Hu, Y., Yuen, K. H., Lazarian, V., et al. 2019d, *Nature Astronomy*, 3, 776, doi: [10.1038/s41550-019-0769-0](https://doi.org/10.1038/s41550-019-0769-0)
- Iroshnikov, P. S. 1963, *AZh*, 40, 742
- Johns-Krull, C. M. 2007, in *Star-Disk Interaction in Young Stars*, ed. J. Bouvier & I. Appenzeller, Vol. 243, 31–42, doi: [10.1017/S1743921307009398](https://doi.org/10.1017/S1743921307009398)
- Kandel, D., Lazarian, A., & Pogosyan, D. 2016, *MNRAS*, 461, 1227, doi: [10.1093/mnras/stw1296](https://doi.org/10.1093/mnras/stw1296)
- . 2017a, *MNRAS*, 464, 3617, doi: [10.1093/mnras/stw2512](https://doi.org/10.1093/mnras/stw2512)
- . 2017b, *MNRAS*, 470, 3103, doi: [10.1093/mnras/stx1358](https://doi.org/10.1093/mnras/stx1358)
- . 2018, *MNRAS*, 478, 530, doi: [10.1093/mnras/sty1115](https://doi.org/10.1093/mnras/sty1115)
- Kolmogorov, A. 1941, *Akademiia Nauk SSSR Doklady*, 30, 301
- Kowal, G., & Lazarian, A. 2010, *ApJ*, 720, 742, doi: [10.1088/0004-637X/720/1/742](https://doi.org/10.1088/0004-637X/720/1/742)
- Kowal, G., Lazarian, A., & Beresnyak, A. 2007, *ApJ*, 658, 423, doi: [10.1086/511515](https://doi.org/10.1086/511515)
- Kraichnan, R. H. 1965, *Physics of Fluids*, 8, 1385, doi: [10.1063/1.1761412](https://doi.org/10.1063/1.1761412)
- Larson, R. B. 1981, *MNRAS*, 194, 809, doi: [10.1093/mnras/194.4.809](https://doi.org/10.1093/mnras/194.4.809)
- Lazarian, A. 2006, *ApJL*, 645, L25, doi: [10.1086/505796](https://doi.org/10.1086/505796)
- Lazarian, A., & Esquivel, A. 2003, *ApJL*, 592, L37, doi: [10.1086/377427](https://doi.org/10.1086/377427)
- Lazarian, A., Eyink, G. L., Jafari, A., et al. 2020, *Physics of Plasmas*, 27, 012305, doi: [10.1063/1.5110603](https://doi.org/10.1063/1.5110603)
- Lazarian, A., HO, K. W., Yuen, K. H., & Vishniac, E. 2023, submitted to *ApJ*, arXiv:2312.05399, doi: [10.48550/arXiv.2312.05399](https://doi.org/10.48550/arXiv.2312.05399)
- Lazarian, A., & Hoang, T. 2007, *MNRAS*, 378, 910, doi: [10.1111/j.1365-2966.2007.11817.x](https://doi.org/10.1111/j.1365-2966.2007.11817.x)
- Lazarian, A., & Pogosyan, D. 2000, *ApJ*, 537, 720, doi: [10.1086/309040](https://doi.org/10.1086/309040)
- . 2004, *ApJ*, 616, 943, doi: [10.1086/422462](https://doi.org/10.1086/422462)
- . 2006, *ApJ*, 652, 1348, doi: [10.1086/508012](https://doi.org/10.1086/508012)
- . 2008, *ApJ*, 686, 350, doi: [10.1086/591238](https://doi.org/10.1086/591238)
- . 2012, *ApJ*, 747, 5, doi: [10.1088/0004-637X/747/1/5](https://doi.org/10.1088/0004-637X/747/1/5)
- . 2016, *ApJ*, 818, 178, doi: [10.3847/0004-637X/818/2/178](https://doi.org/10.3847/0004-637X/818/2/178)
- Lazarian, A., Pogosyan, D., & Esquivel, A. 2002, in *Astronomical Society of the Pacific Conference Series*, Vol. 276, *Seeing Through the Dust: The Detection of HI and the Exploration of the ISM in Galaxies*, ed. A. R. Taylor, T. L. Landecker, & A. G. Willis, 182, doi: [10.48550/arXiv.astro-ph/0112368](https://doi.org/10.48550/arXiv.astro-ph/0112368)
- Lazarian, A., & Vishniac, E. T. 1999, *ApJ*, 517, 700, doi: [10.1086/307233](https://doi.org/10.1086/307233)
- Lazarian, A., & Yuen, K. H. 2018a, *ApJ*, 865, 59, doi: [10.3847/1538-4357/aad3ca](https://doi.org/10.3847/1538-4357/aad3ca)
- . 2018b, *ApJ*, 853, 96, doi: [10.3847/1538-4357/aaa241](https://doi.org/10.3847/1538-4357/aaa241)
- . 2018c, *ApJ*, 865, 59, doi: [10.3847/1538-4357/aad3ca](https://doi.org/10.3847/1538-4357/aad3ca)
- Lazarian, A., Yuen, K. H., Ho, K. W., et al. 2018, *ApJ*, 865, 46, doi: [10.3847/1538-4357/aad7ff](https://doi.org/10.3847/1538-4357/aad7ff)
- Lazarian, A., Yuen, K. H., Lee, H., & Cho, J. 2017, *ApJ*, 842, 30, doi: [10.3847/1538-4357/aa74c6](https://doi.org/10.3847/1538-4357/aa74c6)
- Lazarian, A., Yuen, K. H., & Pogosyan, D. 2022, *ApJ*, accepted for publication, arXiv: 2204.09731, <https://arxiv.org/abs/2002.07996>
- Lithwick, Y., & Goldreich, P. 2001, *ApJ*, 562, 279, doi: [10.1086/323470](https://doi.org/10.1086/323470)
- Lu, Z., Lazarian, A., & Pogosyan, D. 2020, *MNRAS*, 496, 2868, doi: [10.1093/mnras/staa1570](https://doi.org/10.1093/mnras/staa1570)
- Makwana, K. D., & Yan, H. 2020, *Physical Review X*, 10, 031021, doi: [10.1103/PhysRevX.10.031021](https://doi.org/10.1103/PhysRevX.10.031021)
- Malik, S., Yuen, K. H., & Yan, H. 2023, *MNRAS*, 524, 6102, doi: [10.1093/mnras/stad2225](https://doi.org/10.1093/mnras/stad2225)
- . 2024, *ApJ*, 965, 65, doi: [10.3847/1538-4357/ad34d7](https://doi.org/10.3847/1538-4357/ad34d7)
- Mallet, A., Schekochihin, A. A., & Chandran, B. D. G. 2015, *MNRAS*, 449, L77, doi: [10.1093/mnras/slv021](https://doi.org/10.1093/mnras/slv021)
- Maron, J., & Goldreich, P. 2001, *ApJ*, 554, 1175, doi: [10.1086/321413](https://doi.org/10.1086/321413)
- McKee, C. F., & Ostriker, E. C. 2007, *ARA&A*, 45, 565, doi: [10.1146/annurev.astro.45.051806.110602](https://doi.org/10.1146/annurev.astro.45.051806.110602)
- Mestel, L., & Spitzer, L., J. 1956, *MNRAS*, 116, 503, doi: [10.1093/mnras/116.5.503](https://doi.org/10.1093/mnras/116.5.503)
- Meyrand, R., Kiyani, K. H., Gürcan, Ö. D., & Galtier, S. 2018, *Physical Review X*, 8, 031066, doi: [10.1103/PhysRevX.8.031066](https://doi.org/10.1103/PhysRevX.8.031066)
- Montgomery, D., & Turner, L. 1981, *Physics of Fluids*, 24, 825, doi: [10.1063/1.863455](https://doi.org/10.1063/1.863455)

- Mouschovias, T. C., Tassis, K., & Kunz, M. W. 2006, *ApJ*, 646, 1043, doi: [10.1086/500125](https://doi.org/10.1086/500125)
- Oughton, S., Rädler, K.-H., & Matthaeus, W. H. 1997, *Phys. Rev. E*, 56, 2875, doi: [10.1103/PhysRevE.56.2875](https://doi.org/10.1103/PhysRevE.56.2875)
- Pavaskar, P., Yuen, K. H., Yan, H., & Malik, S. 2024, arXiv e-prints, arXiv:2405.17985. <https://arxiv.org/abs/2405.17985>
- Seta, A., Shukurov, A., Wood, T. S., Bushby, P. J., & Snodin, A. P. 2018, *MNRAS*, 473, 4544, doi: [10.1093/mnras/stx2606](https://doi.org/10.1093/mnras/stx2606)
- Skalidis, R., & Tassis, K. 2021, *A&A*, 647, A186, doi: [10.1051/0004-6361/202039779](https://doi.org/10.1051/0004-6361/202039779)
- Stone, J. M., Tomida, K., White, C. J., & Felker, K. G. 2020, *ApJS*, 249, 4, doi: [10.3847/1538-4365/ab929b](https://doi.org/10.3847/1538-4365/ab929b)
- Tofflemire, B. M., Burkhart, B., & Lazarian, A. 2011, *ApJ*, 736, 60, doi: [10.1088/0004-637X/736/1/60](https://doi.org/10.1088/0004-637X/736/1/60)
- Yan, H., & Lazarian, A. 2006, *ApJ*, 653, 1292, doi: [10.1086/508704](https://doi.org/10.1086/508704)
- . 2007, *ApJ*, 657, 618, doi: [10.1086/510847](https://doi.org/10.1086/510847)
- . 2008, *ApJ*, 673, 942, doi: [10.1086/524771](https://doi.org/10.1086/524771)
- Yuen, K. H., Ho, K. W., Law, C. Y., & Chen, A. 2024, *Reviews of Modern Plasma Physics*, *invited review*, arXiv:2404.19101, doi: [10.1007/s41614-024-00156-5](https://doi.org/10.1007/s41614-024-00156-5)
- Yuen, K. H., Ho, K. W., Law, C. Y., Chen, A., & Lazarian, A. 2022, *ApJL*, submitted, arXiv:2204.13760
- Yuen, K. H., Ho, K. W., & Lazarian, A. 2021, *ApJ*, 910, 161, doi: [10.3847/1538-4357/abe4d4](https://doi.org/10.3847/1538-4357/abe4d4)
- Yuen, K. H., & Lazarian, A. 2017a, *ApJL*, 837, L24, doi: [10.3847/2041-8213/aa6255](https://doi.org/10.3847/2041-8213/aa6255)
- . 2017b, arXiv e-prints, arXiv:1703.03026. <https://arxiv.org/abs/1703.03026>
- . 2020a, *ApJ*, 898, 65, doi: [10.3847/1538-4357/ab9307](https://doi.org/10.3847/1538-4357/ab9307)
- . 2020b, *ApJ*, 898, 66, doi: [10.3847/1538-4357/ab9360](https://doi.org/10.3847/1538-4357/ab9360)
- Yuen, K. H., Yan, H., & Lazarian, A. 2023, *MNRAS*, 521, 530, doi: [10.1093/mnras/stad287](https://doi.org/10.1093/mnras/stad287)
- Zhang, H., Chepurinov, A., Yan, H., et al. 2020a, *Nature Astronomy*, 4, 1001, doi: [10.1038/s41550-020-1093-4](https://doi.org/10.1038/s41550-020-1093-4)
- Zhang, J.-F., Hu, K., Cho, J., & Lazarian, A. 2020b, *ApJ*, 895, 20, doi: [10.3847/1538-4357/ab88ac](https://doi.org/10.3847/1538-4357/ab88ac)
- Zhang, J.-F., Lazarian, A., Ho, K. W., et al. 2019, *MNRAS*, 486, 4813, doi: [10.1093/mnras/stz1176](https://doi.org/10.1093/mnras/stz1176)
- Zhao, S., Yan, H., Liu, T. Z., Yuen, K. H., & Shi, M. 2024a, *ApJ*, 962, 89, doi: [10.3847/1538-4357/ad132e](https://doi.org/10.3847/1538-4357/ad132e)
- Zhao, S., Yan, H., Liu, T. Z., Yuen, K. H., & Wang, H. 2024b, *Nature Astronomy*, doi: [10.1038/s41550-024-02249-0](https://doi.org/10.1038/s41550-024-02249-0)